

Cross-Shore Distribution of the Wave-Induced Circulation Over a Dissipative Beach Under Storm Wave Conditions

Marc Pezerat¹ , Xavier Bertin¹, Kévin Martins² , and Laura Lavaud¹ 

¹UMR 7266 LIENSs, CNRS/La Rochelle Université, La Rochelle, France, ²UMR 5805 EPOC, CNRS/Université de Bordeaux, Pessac, France

Key Points:

- Field experiment at a dissipative beach with 6 m H_{m0} at breaking and undertows reaching 0.25 m/s as far as 4 km from the shoreline
- Accurate reproduction of the cross-shore hydrodynamics using a phase-averaged 3D circulation model
- Wave dissipation by breaking locally increases seaward-directed flows by over 100% compared to the surface Stokes drift velocity

Correspondence to:

M. Pezerat,
marc.pezerat@univ-lr.fr

Citation:

Pezerat, M., Bertin, X., Martins, K., & Lavaud, L. (2022). Cross-shore distribution of the wave-induced circulation over a dissipative beach under storm wave conditions. *Journal of Geophysical Research: Oceans*, 127, e2021JC018108. <https://doi.org/10.1029/2021JC018108>

Received 6 OCT 2021
 Accepted 5 MAR 2022

Author Contributions:

Conceptualization: Marc Pezerat, Xavier Bertin, Kévin Martins
Data curation: Marc Pezerat, Xavier Bertin
Funding acquisition: Xavier Bertin
Investigation: Marc Pezerat, Xavier Bertin, Laura Lavaud
Methodology: Marc Pezerat, Xavier Bertin, Kévin Martins
Project Administration: Xavier Bertin
Software: Marc Pezerat, Kévin Martins, Laura Lavaud
Supervision: Xavier Bertin
Validation: Marc Pezerat, Xavier Bertin
Writing – original draft: Marc Pezerat
Writing – review & editing: Xavier Bertin, Kévin Martins, Laura Lavaud

Abstract This study explores the spatial distribution and the driving mechanisms of the wave-induced cross-shore flow within the shoreface and surf zone of a dissipative beach. Unpublished results from a field campaign carried out in early 2021 under storm wave conditions are presented and compared with the predictions from a state-of-the-art phase-averaged three-dimensional circulation modeling system based on the vortex force formalism. Under storm wave conditions, the cross-shore flow is dominated by a strong seaward-directed current in the lower part of the water column. The largest current velocities of this return current are located in the surf zone, where the dissipation by depth-induced breaking is most intense, but offshore-directed velocities up to 0.25 m/s are observed as far as 4 km from the shoreline (≈ 12 m-depth). Numerical experiments further highlight the key control exerted by non-conservative wave forces and wave-enhanced mixing on the cross-shore flow across a transition zone, where depth-induced breaking, whitecapping, and bottom friction all significantly contribute to the wave energy dissipation. Under storm conditions, this transition zone extended almost 6 km offshore and the cross-shore Lagrangian circulation shows a strong seaward-directed jet in the lower part of the water column, whose intensity progressively decreases offshore. In contrast, the surf zone edge appears clearly delimited under fair weather conditions and the seaward-directed current is weakened by a near bottom shoreward-directed current associated with wave bottom streaming in the shoaling region, such that the clockwise Lagrangian overturning circulation is constrained by an additional anti-clockwise overturning cell at the surf zone edge.

Plain Language Summary As waves propagate toward the shore fluid parcels experience a net transport in the direction of wave propagation. This onshore mass transport is compensated by a near bed return flow, which dynamics remain poorly understood. This study combines measurements from a field campaign carried out in early 2021 in front of a gentle sloping beach and numerical modeling to explore the spatial distribution and the driving mechanisms of this wave-induced cross-shore flow. Both observations and model results show that the largest current velocities of this return current are located very close to the shoreline, where the wave breaking is the most intense, but values up to 0.25 m/s are observed as far as 4 km from the shoreline under storm conditions. Numerical experiments further highlight the key control exerted by the wave forces and the wave-enhanced mixing, which induce very contrasted circulation patterns under fair weather or storm conditions and strongly constrain the vertical structure of the cross shore flow.

1. Introduction

The nearshore circulation driven by breaking waves contributes to the cross-shelf transport of material, especially in the vicinity of the surf zone, such as the transport of nutrient (e.g., Morgan et al., 2018) or sediment, which can result in large morphological changes under storm conditions (e.g., Castelle et al., 2015; Coco et al., 2014; Wright & Short, 1984).

Considering a weak along-shore variability of the topography and a shore normal incidence of waves, the interplay between waves and currents most notably drives the so-called undertow. Based on the depth-integrated continuity equation, the undertow commonly designates the time- and depth-averaged Eulerian offshore flow compensating for the onshore mass transport associated with the Stokes drift. The onshore-directed mass transport is further enhanced within the surf zone due to contribution from surface wave rollers (e.g., Svendsen, 1984a). The underlying dynamics were further investigated both theoretically and experimentally, providing some insights onto the vertical structure of the (Eulerian) cross-shore flow. Within the surf zone, several pioneering studies (e.g., Deigaard et al., 1991; Garcez Faria et al., 2000; Haines & Sallenger, 1994; Stive & Wind, 1986; Svendsen, 1984a,

among many others) proposed theoretical models, which all conceptually rely on the local imbalance between the depth-uniform barotropic pressure gradient associated with the wave setup and the depth-varying gradient of the wave radiation stresses. These models adequately predict parabolic velocity profile, whose curvature is a function of local wave quantities and the vertical eddy viscosity (e.g., Garcez Faria et al., 2000).

In contrast, the wave induced dynamics seaward of the surf zone received much less attention, particularly under storm waves. Most notably, Lentz et al. (2008) combined long term observations with a one-dimensional vertical model adapted from Xu and Bowen (1994) to study the vertical structure of the cross-shore flow up to the inner-shelf. These authors showed that the cross-shore velocity profiles seaward of the surf zone do not resemble the parabolic profiles observed within the surf zone, but exhibit a maximum near the surface, which is consistent with a balance between the Coriolis force associated with the offshore flow and the Stokes-Coriolis force, also referred to as the Hasselmann wave stress (Hasselmann, 1970). As a result, the offshore flow tends to be equal in magnitude but opposite in direction to the onshore Stokes drift velocity all along the water column, which implies a nearly depth-uniform zero cross-shore Lagrangian flow seaward of the surf zone.

In recent years, wave-averaged three-dimensional (3D) circulation models have been developed aiming to represent consistently the effect of short waves on the mean circulation for a wide range of nearshore, coastal and open-ocean applications. Several theoretical approaches were proposed on the form of the wave-modified primitive equations that would be suitable for such models (e.g., see Bennis et al., 2011). The wave-averaged vortex force formalism, which separates conservative and non-conservative wave forcing on the 3D quasi-Eulerian mean circulation, constitutes a theoretically robust framework employed within several of these modeling systems (e.g., Delpy et al., 2014; Guérin et al., 2018; Kumar et al., 2012; Michaud et al., 2012; Uchiyama et al., 2010; Zheng et al., 2017). For nearshore applications, non-conservative effects associated with wave energy dissipation processes through depth-induced breaking, whitecapping and bottom friction are expected to play a crucial role. While Smith (2006) consistently derived the contribution of these processes to the depth-integrated momentum equations, no definite theory exists to express these terms for the depth-resolving equations. In particular, it is assumed that the dissipation of wave energy by breaking acts either like a surface stress on the mean flow or like a body force, in which case one can thus impose an empirical vertical distribution such that the breaking contribution applies at appropriate depths near the surface (e.g., Uchiyama et al., 2010). As pointed out by Rasche (2007), the wave-enhanced vertical mixing associated with the production of turbulence by breaking waves mostly controls the vertical shear of the horizontal current velocity so that the near-surface distribution of the momentum source sparsely matters. In this regard, wave-averaged 3D circulation models are usually supplemented by a two-equation turbulence closure model, which allows to approximate the wave-enhanced turbulent kinetic energy (TKE) budget across the water column. There is a consensus in the literature to model the TKE injection with a flux-type boundary condition at the water surface assuming a power law for the decay of TKE (Umlauf & Burchard, 2003). Craig and Banner (1994) proposed to express the surface flux of energy injected into the water column in proportion to the surface wind friction velocity cubed. Following this approach, it is assumed that the energy flux from the wind to the wavefield very closely matches that transferred from the wavefield to the water column, which appears especially relevant for the deep ocean where breaking processes (whitecapping) significantly impacts the atmospheric drag coefficient. For nearshore applications however, observations support the fact that the surface flux of TKE scales with the energy dissipated through depth-induced breaking (e.g., Feddersen & Trowbridge, 2005). It is also interesting to note that the decay of TKE near the surface is particularly sensitive to the surface mixing length, which remains an empirically parameterized quantity (e.g., see Moghimi et al., 2016).

Among the above mentioned studies, Kumar et al. (2012), Michaud et al. (2012), Uchiyama et al. (2010) and Zheng et al. (2017) essentially detailed the implementation of the vortex force formalism within various modeling framework and further aimed to demonstrate the general applicability of this approach to study surf zone dynamics over commonly used study cases, including applications at Duck, N.C., which serves as a reference benchmark. In addition, Kumar et al. (2012) also reproduced the results from Lentz et al. (2008) seaward of the surf zone using the same data set. In a recent model-based study following Uchiyama et al. (2010), Wang et al. (2020) further discussed the effect of the bottom wave streaming, which is the stress along the direction of wave propagation that accompanies the wave energy dissipation by bottom friction. Most notably, their results tended to show that the Lagrangian overturning circulation within the surf zone could be substantially weakened by an opposite overturning cell arising seaward of the surf zone and extending within it, associated with the bottom

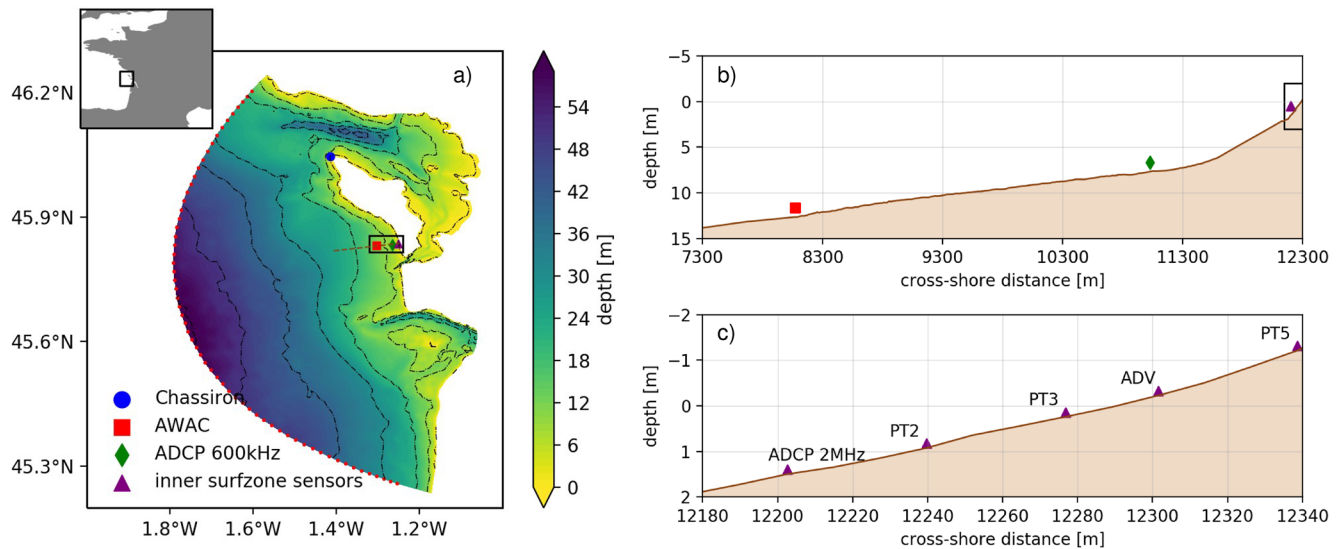


Figure 1. (a) Location of the study area in the Bay of Biscay, bathymetric map covering the computational domain (the open boundary is symbolized with the red dotted line) with isobaths reduced to the mean sea level displayed every 10 m (black dash-dotted lines), and position of the Chassiron meteorological station, AWAC, Acoustic Doppler Current Profilers (ADCP) 600 kHz and inter-tidal area sensors. A cross-shore profile extending from the isobath 25 m to PT5 sensor is also displayed (brown dashed line). (b) Cross-shore profile from AWAC location to the first sensor deployed within the inter-tidal area. (c) Zoom on inter-tidal area sensors.

wave streaming. Realistic applications of state-of-the-art, fully coupled, wave-averaged 3D circulation models in the nearshore region remain very scarce (Delpy et al., 2014; Guérin et al., 2018; Michaud et al., 2012), especially under storm conditions, such that our comprehensive understanding of the wave-induced hydrodynamics remains somehow limited and the predictive skills of these models uncertain.

This study aims to explore the cross-shore distribution and the driving mechanisms of the wave-induced cross-shore circulation within the shoreface and the surf zone of a dissipative beach. We present unpublished results from a field campaign carried out in early 2021 in the central part of the French Atlantic coast under storm wave conditions, complemented with predictions from the state-of-the-art 3D circulation model SCHISM (Zhang et al., 2016), fully coupled with the spectral wave model WWM (Roland et al., 2012). The manuscript is organized as follows. The study area, the field campaign and the processing of in-situ measurements are presented in Section 2. The parameterization of the modeling system is detailed in Section 3 and its predictive skills are assessed in Section 4 for the case study considered here. The Section 5 discusses the contrasted wave-induced circulation patterns and associated driving mechanisms under high and moderate wave energy conditions based on further numerical experiments. Finally, concluding remarks are provided in Section 6.

2. Study Area and Field Campaign

2.1. Study Area

The study area is located along the South-Western coast of the Oléron Island in the central part of the French Atlantic coast (see Figure 1a), in front of Saint-Trojan Beach. This beach corresponds to a 8 km-long sandspit bounded to the South by the Maumusson Inlet and to the North by a rocky shore platform (Lavaud et al., 2020). In this region, tides are semi-diurnal and range from 1.5 to 5.5 m, which corresponds to a macrotidal regime. Yearly mean wave conditions along the 30 m isobath are characterized by a significant wave height of 1.6 m, a mean wave period of 5.9 s and a direction of 285° from the true North (Dodet et al., 2019), but the offshore significant wave height can exceed 10 m with peak periods over 20 s (Bertin et al., 2015). This area is characterized by a very gently sloping shoreface (the isobath 20 m being found approximately 10 km offshore) and a non-barred dissipative beach composed of fine sandy sediments and exposed to an energetic wave climate. Although this stretch of coast is relatively along-shore uniform, small amplitude inter-tidal bars can develop after the persistence of fair weather conditions (see Bertin et al., 2008; Guérin et al., 2018, for supplementary studies in this area).

2.2. Field Campaign and Data Processing

The field campaign was carried out between January and February 2021 in two steps. First, two Acoustic Doppler Current Profilers (ADCP) were mounted on structures anchored in the seabed, at approximately 12.5 and 7.5 m-depth locations below Mean Sea Level (MSL) for a long-term deployment between the January 19 and the February 26 (see Figure 1). The most offshore instrument is a high resolution ADCP (1 MHz) integrating an Acoustic Surface Tracker (AST) and is hereafter referred to as the AWAC, whereas the other one is a medium-resolution ADCP (600 kHz). Both instruments alternated a “current cycle” and a “wave cycle” each hour. During the “current cycle,” 10 min-averaged velocity profile measurements were collected along the vertical axis, whereas during the “wave cycle” velocity measurements within a fixed 2 m-high cell and pressure measurements were performed at 2 Hz during 20 min. Second, a set of sensors was deployed in the inter-tidal area (Figure 1c) between January 29th and the 31st during spring tides so as to capture a highly energetic event associated with the storm Justine. The offshore significant wave height at the Biscay Buoy location (5°W, 45.23°N) reached 10 m, which corresponds to a return period of the order of 1 year (Nicolae-Lerma et al., 2015). The swell associated with the storm reached the study area during the night of the 30th from a westward direction, while local winds reached 15 m/s at the storm peak. This set of sensors was deployed along a cross-shore profile and included one 2 MHz ADCP (with a similar data collection scheme than for the two offshore ADCPs), three pressure transducers with a 2 Hz sampling frequency (PT) and one Acoustic Doppler Velocimeter deployed 20 cm above the seabed, with a 16 Hz sampling frequency (ADV). The PTs and ADV all performed continuous measurements.

For each sensor, sea-bottom pressure timeseries were split into 20 min-long bursts (consistent with ADCPs “wave cycle”), corrected for sea level atmospheric pressure using data collected at the nearby meteorological station of Chassiron (Figure 1a), detrended and converted into a sea-surface elevation signal assuming a hydrostatic pressure. For the sensors deployed in the inter-tidal area, measurements below a burst-averaged water depth of 0.5 m were discarded due to the presence of substantial infra-gravity waves, which caused the sensors to be intermittently dry. Then, pressure attenuation with depth due to non-hydrostatic effects was corrected using the Transfer Function Method based on the linear wave theory (TFM, e.g., Bishop & Donelan, 1987). This method requires an upper cutoff frequency to remove high frequency noise that is amplified by the TFM correction, and to prevent the over-amplification of high-frequency energy levels due to non-linear interactions in intermediate and shallow-water depths (Mouragues et al., 2019). The cutoff frequency was set to 0.2 Hz for the two offshore sensors and 0.4 Hz for the sensors in the inter-tidal area. Finally, the sea surface elevation density spectra $E(f)$ were computed by means of a Fast Fourier Transform on 10 Hanning-windowed segments with a 50% overlap, which allows a good compromise between statistical stability (20 degrees of freedom) and frequency resolution (8.3 mHz). The processing of pressure measurements was further verified at the AWAC location by comparing the sea-surface elevation spectra with those obtained from the AST measurements. These measurements were not used directly due to spurious signals during the most energetic events, whose are probably explained by the presence of air bubbles in the water column induced by the breaking of storm waves (not shown). Wave bulk parameters (significant wave height, H_{m0} , mean and continuous peak periods, T_{m02} and T_{pc}) were computed using the p^{th} moments of the spectra:

$$m_p = \int_{f_{\min}}^{f_c} f^p E(f) df \quad (1)$$

such that:

$$\begin{aligned} H_{m0} &= 4\sqrt{m_0} \\ T_{m02} &= \sqrt{\frac{m_0}{m_2}} \\ T_{pc} &= \frac{m_{-2}m_1}{m_0^2} \end{aligned} \quad (2)$$

For each sensor, an adaptive f_{\min} value, defined as half the continuous peak frequency computed at the AWAC location, was used in order to separate the gravity from the infra-gravity bands (e.g., Bertin et al., 2020; Hamm & Peronnard, 1997).

For the two offshore ADCPs, 10 min-averaged vertical profiles of current velocities were acquired along bins spanned respectively every 1 m (AWAC) and 0.5 m (ADCP 600 kHz). The measurements above a distance equal to the water depth minus half the significant wave height were discarded due to contamination by surface reflections from the sidelobes of the ADCP acoustic pulses (Appell et al., 1991). Current velocity profile measurements from the ADCP 2 MHz deployed in the inter-tidal area were discarded because of spurious bin-to-bin velocity differences. Finally, continuous velocity measurements from the ADV, were split into 30 min-long bursts and filtered from spikes using the phase-space thresholding method of Goring and Nikora (2002).

The inter-tidal topography was surveyed at low tide during the deployment (29/01/2021) and the recovery (31/01/2021) of the instruments with PPK GNSS over an area centered on the instrumented transect and extending 1 km along-shore. The comparison between both datasets showed very limited morphological changes (with a root mean square difference of 0.10 m along the instrumented profile), a behavior already reported by Guérin et al. (2018) under similar storm wave conditions. The subtidal bathymetry was surveyed at the location of the instrumented profile up to a water depth of 11 m below MSL four weeks after the deployment in the inter-tidal area by means of a Norbit multi-beam echo-sounder. This bathymetric data set was merged with an extensive single-beam echo-sounder survey carried out in April 2013. Both datasets in the region where they overlap show a smooth transition in the subtidal zone with changes of the order of 0.4 m.

3. Modeling System

The modeling system used in this study couples the 3D circulation model SCHISM (Zhang et al., 2016) and the third generation spectral wave model WWM (Roland et al., 2012). This modeling system offers the flexibility to cover large geographic areas with unstructured grid and very robust numerical schemes for both models. The 3D wave-induced circulation is modeled through the vortex force formalism, such as presented by Bennis et al. (2011). Its detailed implementation in SCHISM can be found in Guérin et al. (2018) and is recalled in Appendix A. In the following, only the parameterization of the relevant part of the model and further improvements since Guérin et al. (2018) are described.

3.1. Parameterization of WWM

3.1.1. Depth-Induced Breaking Parameterization

The wave energy dissipation rate by depth-induced breaking is computed according to the model of Battjes and Janssen (1978) with an adaptive breaking coefficient (B) as proposed by Pezerat et al. (2021). The local mean (phase-averaged) rate of energy dissipation per unit area D_{db} in (W/m^2) reads:

$$D_{db} = \frac{B}{4} \rho g f_{mean} Q_b H_m^2 \quad (3)$$

where $B = 40 \tan \beta$, with $\tan \beta$ the local bottom slope; f_{mean} is a mean frequency, usually computed as the ratio m_1/m_0 (see Equation 1); Q_b is the local fraction of breaking (and broken) waves and H_m is the local maximum possible wave height estimated by means of a parameterized Miche-type breaking criterion. Under the shallow water assumption, H_m reads:

$$H_m = \gamma h \quad (4)$$

where γ is the breaking index, an adjustable coefficient, usually kept constant at 0.73 following the calibration performed by Battjes and Stive (1985). However, as pointed out by Pezerat et al. (2021), the introduction of the adaptive breaking coefficient requires a newly calibrated breaking index. Based on sensitivity tests performed with the model on H_{m0} results considering the entire data set (not shown), a constant value of $\gamma = 0.60$ was considered for this study. It is worth noting that this value might show some site- or wave conditions-specificity, but it is not the purpose of this study to propose an extensive calibration of the breaking index. Finally, following the approach of Eldeberky and Battjes (1996), the corresponding source term in WWM is computed by distributing D_{db} over frequencies and directions in proportion to the spectral action density:

$$S_{db} = -\frac{D_{db}}{E_{tot}} N \quad \text{where} \quad E_{tot} = \rho g \int_{\sigma} \int_{\theta} E d\sigma' d\theta' \quad (5)$$

3.1.2. Other Source Terms

The wind input (S_{in}) and dissipation by whitecapping (S_{ds}) are formulated according to the parameterization of Ardhuin et al. (2010). Non-linear quadruplet interactions ($S_{nl,4}$) are taken into account following the approach of Hasselmann et al. (1985), whereas the non-linear triad interactions ($S_{nl,3}$) are parameterized following the approach of Eldeberky (1997). Finally, the formulation of the energy dissipation by bottom friction (S_{bf}) is adapted from Tolman (1994). This formulation is based on the model of Madsen et al. (1988) with a parameterization of the roughness issued from Grant and Madsen (1982), and was subsequently adapted by Ardhuin et al. (2003) based on the SHOWEX experiment.

3.2. Parameterization of SCHISM

3.2.1. Non-Conservative Wave Forces

The non-conservative wave forcing due to wave breaking [$\hat{F}_{br,x}, \hat{F}_{br,y}$] includes the effect of whitecapping and depth-induced breaking further modified due to the action of wave rollers (cf., Appendix A for the description of the roller model):

$$[\hat{F}_{br,x}, \hat{F}_{br,y}] = \frac{\delta_{z,\bar{\eta}}}{\rho} \left(- \int_{\sigma} \int_{\theta} k ((1 - \alpha_R) S_{db} + S_{ds}) [\cos\theta', \sin\theta'] d\sigma' d\theta' + \frac{D_R}{\sigma_p} k_p [\cos\theta_m, \sin\theta_m] \right) \quad (6)$$

where the vertical distribution function is given by a delta function $\delta_{z,\bar{\eta}}$, such that the breaking-induced momentum is injected within the first cell below the free surface (Bennis et al., 2011). The roller model shows barely any effect at both offshore locations, while the current intensity slightly increases with α_R at the ADV location (not shown). The model best-fit results were obtained with $\alpha_R = 0.5$.

The bottom streaming corresponds to the stress along the direction of wave propagation that accompanies the dissipation of wave energy by bottom friction within the wave boundary layer (Longuet-Higgins, 1953). The corresponding body force [$\hat{F}_{ws,x}, \hat{F}_{ws,y}$] is formulated by means of an upward decaying vertical distribution of the wave energy dissipation by bottom friction (Uchiyama et al., 2010):

$$[\hat{F}_{ws,x}, \hat{F}_{ws,y}] = - \frac{f^{ws}(z)}{\rho} \int_{\sigma} \int_{\theta} k S_{bf} [\cos\theta', \sin\theta'] d\sigma' d\theta' \quad (7)$$

where f^{ws} is a vertical distribution function given by:

$$f^{ws}(z) = \frac{1 - \tanh(k_{wd}(d+z))^2}{\int_{-d}^{\bar{\eta}} 1 - \tanh(k_{wd}(d+z))^2 dz} \quad (8)$$

where $1/K_{wd} = a_{wd}\delta_{wbl}$ is a decay length proportional to the wave boundary layer thickness (δ_{wbl}). Within SCHISM, δ_{wbl} is derived from the wave boundary layer model of Madsen (1995) that is used to compute the apparent roughness length for the parameterization of the bottom friction within the circulation model (Section 3.2.3). The proportionality coefficient a_{wd} is taken equal to unity, such that the decay length matches the theoretical wave boundary layer thickness for monochromatic waves although laboratory measurements of the bottom boundary layer under random waves suggest a significant increase in the thickness, that is, $a_{wd} > 1$ (Klopman, 1994).

3.2.2. Wave-Enhanced Turbulence at the Surface

The circulation model is supplemented by a $K - \omega$ turbulence closure model retrieved from the Generic Length Scale (GLS) two-equation turbulence closure model within the framework of the General Ocean Turbulence Model (GOTM, Burchard et al., 1999; Umlauf et al., 2005). At the water surface, the turbulence closure model accounts for a TKE injection by breaking waves (K in m^2/s^2) through a flux-type boundary condition assuming a power law for the vertical decay of K (Umlauf & Burchard, 2003), which reads:

$$\frac{\nu}{\sigma_K} \frac{\partial K}{\partial z} = F_K \left(\frac{z_0^s - z'}{z_0^s} \right)^{\frac{3}{2}\alpha} \quad \text{at } z = \bar{\eta} \quad (9)$$

where F_K (in m^3/s^3) is the surface flux of energy injected into the water column, ν is the vertical eddy viscosity, σ_K is the turbulent Schmidt number for K , α is the spatial decay rate of TKE in the wave enhanced layer, z_0^s is the surface mixing length and z' is the distance below the surface at which the flux is imposed. For numerical reason, z' is prescribed as half the height of the top cell, such that the boundary condition for K requires a refined discretization of the vertical grid near the surface. The surface mixing length (z_0^s) controls the depth of penetration for the injected TKE. There are strong uncertainties over this quantity, which has been either parameterized as a constant (e.g., $z_0^s = 0.2$ m, Feddersen & Trowbridge, 2005) or as a function of the significant wave height: $z_0^s = \alpha_w H_{m0}$, with $\alpha_w = \mathcal{O}(1)$ (see Moghimi et al., 2016, for a short review). Following the approach of Feddersen and Trowbridge (2005), the surface flux of TKE injected at the surface scales with the energy dissipated through wave-related processes at the surface:

$$F_K = \frac{c_{db}}{\rho} \left(-(1 - \alpha_R) \int_{\sigma} \int_{\theta} \sigma' S_{db} d\sigma' d\theta' + D_R \right) - \frac{c_{ds}}{\rho} \int_{\sigma} \int_{\theta} \sigma' S_{ds} d\sigma' d\theta' \quad (10)$$

where the coefficients C_{db} and C_{ds} control the amount of energy injected to the water column. The range of value 0.01–0.25 has been proposed in the literature for C_{db} (e.g., Feddersen, 2012a, 2012b; Feddersen & Trowbridge, 2005; Huang et al., 2009), while Paskyabi et al. (2012) suggest $C_{ds} \simeq 1$. The model best-fit results were obtained with $z_0^s = \alpha_w H_{m0}$, $\alpha_w = 1$; $C_{db} = 0.15$ and $C_{ds} = 1$.

3.2.3. Bottom Boundary Condition

The bottom boundary condition imposes a balance between the internal Reynolds stress and the bottom frictional stress: $[\tau_{b,x}, \tau_{b,y}]$

$$\nu \frac{\partial [\hat{u}, \hat{v}]}{\partial z} = \frac{[\tau_{b,x}, \tau_{b,y}]}{\rho} \quad \text{at } z = -d \quad (11)$$

The law of the wall is then assumed, leading to a logarithmic profile for the velocity within a constant stress layer that presumably contains the bottom cell while the bottom stress is formulated with a quadratic bottom drag parameterization. The bottom stress finally reads (e.g., Blumberg & Mellor, 1987):

$$[\tau_{b,x}, \tau_{b,y}] = \rho C_d \sqrt{\hat{u}_b^2 + \hat{v}_b^2} [\hat{u}_b, \hat{v}_b] \quad \text{with } C_d = \left(\frac{\kappa}{\ln \left(\frac{\delta_b}{z_0} \right)} \right)^2 \quad (12)$$

where C_d is the friction factor, $[\hat{u}_b, \hat{v}_b]$ is the velocity at the top of the bottom computational cell, κ is the von Kármán's constant, δ_b is the thickness of the bottom cell (in m) and Z_0 is the bottom roughness length (in m). In the presence of waves, the wave-current interaction theory by Madsen (1995) as modified by Mathisen and Madsen (1999) is applied to compute an apparent roughness length z_0^a , which further replaces Z_0 in the expression of C_d , and thus allows to account for the enhanced roughness experienced by the current in presence of waves. This approach takes as input a (physical) bottom roughness length (Z_0) to provide an expression of the wave boundary layer thickness and z_0^a following a numerical procedure described in H. Zhang et al. (2004). In this study, Z_0 varies spatially between 0.1 and 5 mm to account for the seabed granulometric variability based on the sea-bottom nature map provided by the Hydrographic and Oceanographic French Office.

3.3. Model Implementation

The coupling between SCHISM and WWM is made at the source code level. Both models share the same unstructured grid and domain decomposition. The horizontal spatial resolution ranges from 2 km at the offshore boundary down to 20 m in the surf zone. The vertical grid for the circulation model is discretized using 25 S-levels stretched near the surface and the bottom. The time step for the circulation model is set to 10 s whereas WWM is running in implicit mode (Abdolali et al., 2020; Booij et al., 1999). This allows to relax the constraint for the time step of the wave module, which was set to 300 s. Finally, the spectral space in WWM was discretized in 36 directions covering the entire trigonometric circle and 24 frequencies ranging from 0.03 to 0.4 Hz.

At the domain offshore boundaries, the tidal forcing was computed considering the 16 main constituents linearly interpolated from the regional tidal model of Bertin et al. (2012), whereas WWM was forced with timeseries of energy spectra obtained from a North Atlantic application of the spectral wave model WaveWatch III (WW3, Tolman, 1991). For both SCHISM and WWM, the atmospheric forcing consisted of MSL pressure and wind speed at 10 m issued from the meteorological operational model ARPEGE (e.g., Déqué et al., 1994), interpolated onto a 0.1° regular grid. WW3 was forced with wind fields at 10 m originating from the Climate Forecast System Reanalysis (CFSR, Saha et al., 2011) extracted from a 0.2° regular grid covering the entire North Atlantic basin. ARPEGE was preferred to CFSR for our local application of the modeling system considering its slightly improved predictive skills as compared to measurements of wind speed and direction at the nearby meteorological station of Chassiron (Figure 1).

4. Observations and Predictive Skills of the Model

A comparison between measurements and model best-fit results (run Rref) is presented. The overall model performance for each quantity is assessed with the normalized bias (NB) and the normalized root mean square error (NRMSE):

$$\text{NB}(X) = \begin{cases} \frac{\overline{\hat{X}} - \overline{X}}{(\max X - \min X)} \times 100 & \text{if } \overline{X} \simeq 0 \\ \frac{\overline{\hat{X}} - \overline{X}}{\overline{X}} \times 100 & \end{cases} \quad (13)$$

$$\text{NRMSE}(X) = \begin{cases} \frac{\sqrt{(\hat{X} - X)^2}}{(\max X - \min X)} \times 100 & \text{if } \overline{X} \simeq 0 \\ \sqrt{\frac{(\hat{X} - X)^2}{X^2}} \times 100 & \end{cases} \quad (14)$$

where X and \hat{X} respectively correspond to the measured and modeled quantity and the overbar denotes the average over the timeseries.

4.1. Water Levels and Short Waves

Phase-averaged surface elevation variations are very well reproduced by the model at the AWAC and ADCP 600 kHz locations (Figures 2a and 2b), with a NRMSE lower than 6% obtained at both locations. The negative bias observed at the AWAC location (NB = -4.1%) could be attributed to pressure sensor drift, as it increases in time while such bias is not observed at the nearby ADCP 600 kHz location. Model results on short waves are compared to observations by means of bulk parameters computed with moments integrated over the same frequency range as the data. These are very well reproduced by the model at both locations (Figures 2c–2h) with a NRMSE on both H_{m0} and T_{m02} below 7%, only the continuous peak period is slightly underestimated at the storm peak, resulting in a negative NB of -7.3% at the ADCP 600 kHz location. This problem might be explained by the fact that spectral wave models allow to represent energy transfers toward higher harmonics by sum self interactions with the LTA formulation of (Eldeberky, 1997) but not by difference interactions. Thus, the model cannot represent transfers from the gravity band toward the IG band and the subsequent transfers back to the gravity band by the generation of IG wave higher harmonics (e.g., Bertin et al., 2020), nor direct transfers toward low frequencies in the gravity band (e.g., De Bakker et al., 2015). Both field measurements at the ADCP 600 kHz location and model results show that H_{m0} is tidally modulated when exceeding approximately 2 m at the AWAC location (Figure 2d). Such modulation also occurs at the storm peak at the AWAC location ($H_{m0} \simeq 6$ m, Figure 2c). This clearly suggests that depth-induced breaking starts being substantial as far as 4 km away from the shoreline ($\simeq 12.5$ m-depth) under energetic conditions. In addition T_{m02} period is also tidally modulated, highlighting the significant contribution of the non-linear triad interactions, whose intensity varies with the water-depth. As the water-depth decreases, more energy is transferred toward the higher harmonics by non-linear triad interactions,

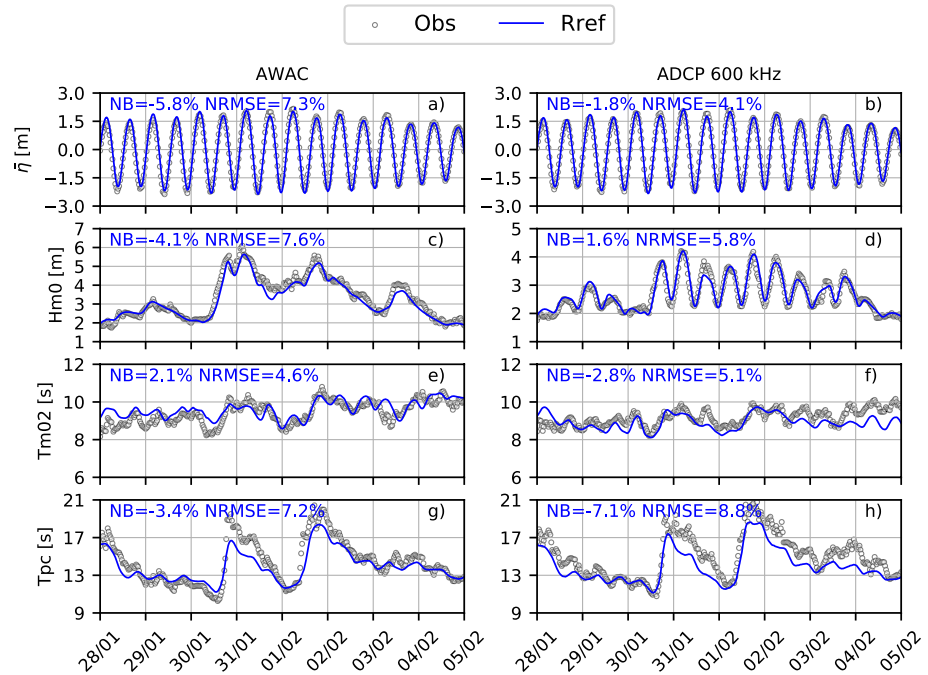


Figure 2. Measured and simulated phase-averaged free surface elevation ($\bar{\eta}$), significant wave height (H_{m0}), mean period (T_{m02}) and continuous peak period (T_{pc}) timeseries at the AWAC (left panels) and Acoustic Doppler Current Profilers (ADCP) 600 kHz (right panels) locations using the configuration of reference (Rref).

such that T_{m02} decreases. Within the inter-tidal area most of the differences between model results and measurements are observed for water-depths below 1 m (see Figure 3). Water levels and significant wave heights are well reproduced by the model with a NRMSE computed over all sensors that respectively reaches 10.4% and 10.8%. The T_{m02} period is not shown because a significant amount of energy is transferred toward the IG band, which can partly go back to the gravity band through the generation of IG wave higher harmonics (Bertin et al., 2020), resulting in an increase of T_{m02} , a process that cannot be reproduced by the phase-averaged model.

4.2. Cross-Shore Circulation

The model results for Rref on the cross-shore velocity component show a fairly good agreement with measurements from the AWAC and the ADCP 600 kHz as shown Figure 4 below the lowest sea surface tidal level. Overall, the NRMSE varies between 13.9% and 20%, while the NB fluctuates between -2.9% and 5.6% . Note, however, that measurements from the ADCP 600 kHz are more scattered under energetic wave conditions. First, this might be partly due to measurement artifacts associated with the generation of bubbles in the water column by depth-induced breaking, which is particularly active at this location (cf. Section 4.1). Second, as vertical current profile measurements are 10 min-averaged, there may be an aliasing of the signal associated with currents induced by IG waves, whose period can exceed 300 s at this beach under storm conditions (Bertin et al., 2020). As averaging currents over a longer period within a thicker cell results in a more accurate measurement of the current velocity, we arbitrarily discarded current profile velocity measurement that departed by more than 0.15 m/s from the 20 min-averaged velocity measurement performed during the wave cycle within the fixed 2 m-high cell (see the red triangles in Figure 4). Both model results and measurements clearly show that the cross-shore velocity is mostly offshore-directed under energetic wave conditions reaching almost -0.5 m/s at the AWAC location around the 31/01/2021. The model results for a run performed without waves (Rnowave), which only accounts for the tides and the atmospheric forcing, show a strong positive bias at both locations (e.g., the NB reaches 27.3% at the ADCP 600 kHz location), so that the comparison between Rref and Rnowave highlights the significant contribution of the wave-induced current to the cross-shore flow. Based on this comparison, the contribution of the wave-induced current at the peak of the storm reaches as much as 0.25 m/s.

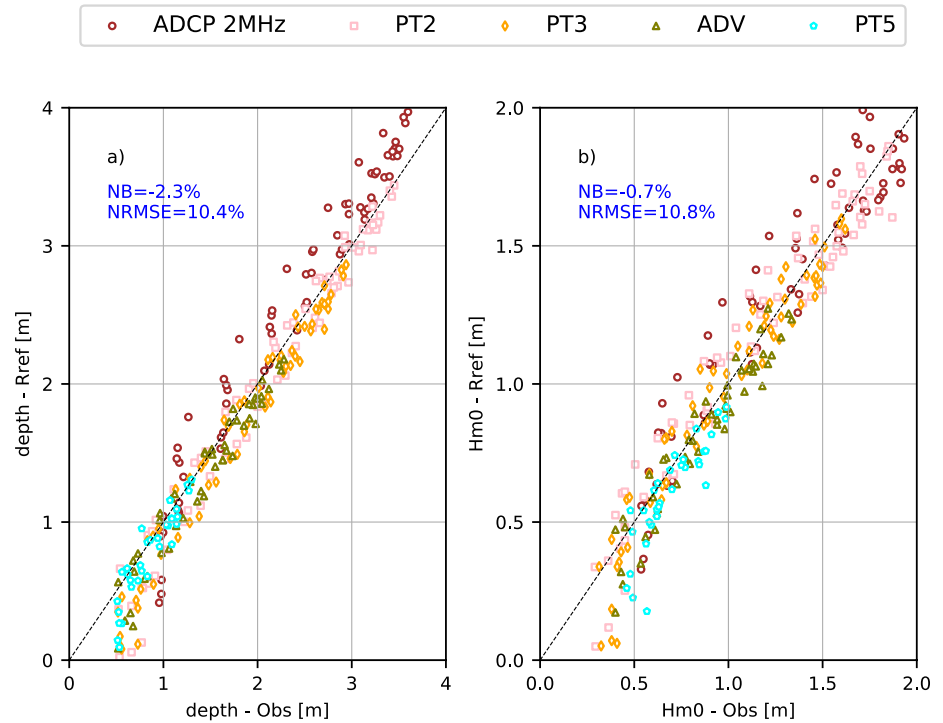


Figure 3. Scatter plot of the measured and simulated water depth (panel a) and significant wave height (H_{m0} , panel b) at the inner surf zone sensors locations using the configuration of reference (Rref).

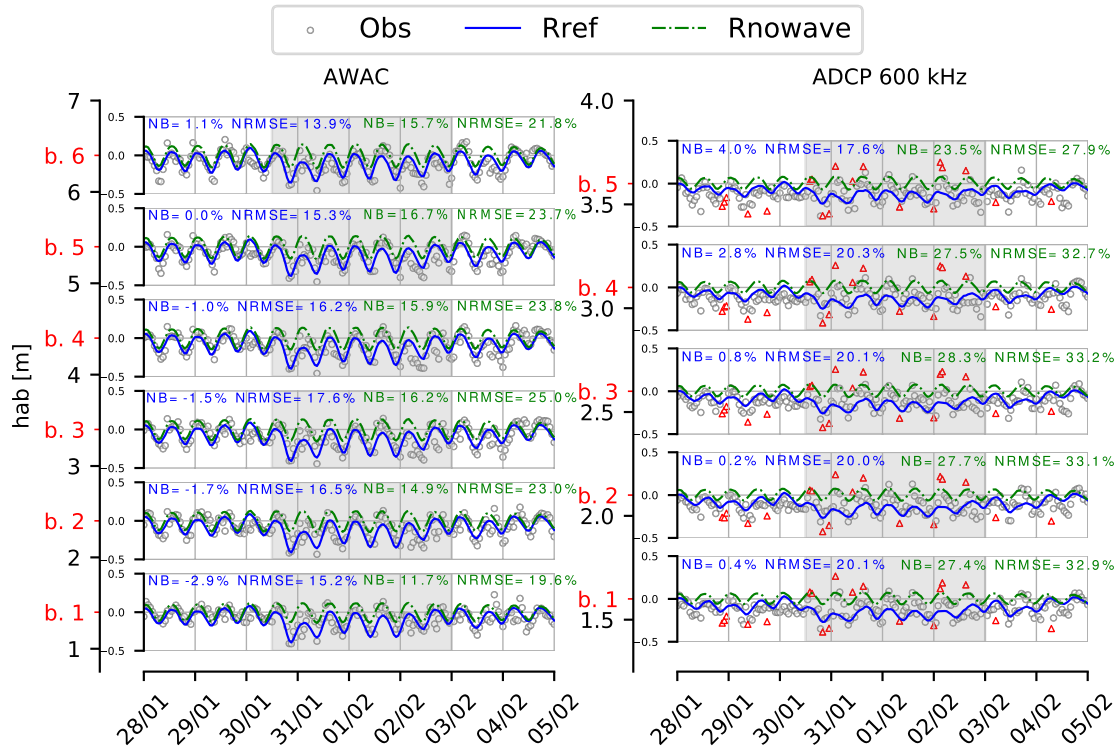


Figure 4. Measured and simulated cross-shore velocity component timeseries at the AWAC (left panel) and Acoustic Doppler Current Profilers (ADCP) 600 kHz (right panel) locations displayed for each vertical bin below the sea surface lowest level. Model results are presented for the run of reference (Rref) and for a run performed without waves (Rnowave). Red triangles tag the discarded measurements. The vertical position of each bin (denoted b) is measured from the bottom and hab stands for height above the sea-bed. The time range of the storm event is delimited by the gray background.

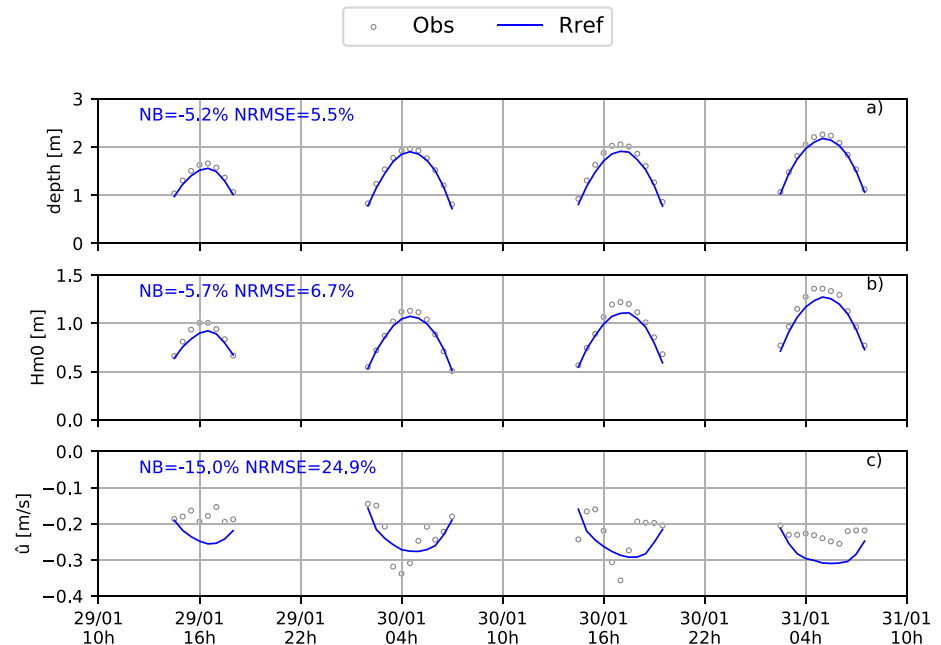


Figure 5. Measured and simulated water depth (panel a), significant wave height (H_{m0} , panel b) and cross-shore velocity component timeseries (\bar{u} , panel c) at the Acoustic Doppler Velocimeter location.

At the ADV location, burst-averaged cross-shore velocity measurements are quite scattered, especially during the second and third tidal cycle with fluctuations reaching 0.2 m/s. The 30-min averaged current velocities suggest the presence of Very Low Frequency oscillations (VLF, frequencies below 4 mHz), while IG waves contribution was presumably filtered. The analysis of the whole data set revealed that waves were mostly normally incident during the storm event, which is quite common during energetic event at this site (Bertin et al., 2008). As a consequence, mean longshore currents remained weak during the field campaign (ranging from -0.10 to 0.15 m/s) and were alternatively northward and southward-directed within a very wide surf zone (not shown). Shear instabilities of mean longshore currents, which require the presence of a strong shear (e.g., associated with highly oblique large waves breaking over a bar, see Noyes et al., 2004; Oltman-Shay et al., 1989) cannot therefore explain such VLF motions. Instead, it could be attributed to the breaking of energetic wave groups that has been identified as a mechanism for the generation of surf zone eddies through the generation of vorticity at the scale of individual waves or wave groups (Feddersen, 2014; Long & Özkan-Haller, 2009), which is then transferred to VLF frequencies and larger spatial scales through non-linear inverse energy cascades (Elgar & Raubenheimer, 2020; Feddersen, 2014).

These complex dynamical features cannot be reproduced by the present phase-averaged modeling approach, which undermines the comparison with the field observations (the NRMSE on the cross-shore velocity component reaches 24.9%). Both model results and observations qualitatively show that the cross-shore velocity component is dominated by a wave-induced seaward-oriented current, whose intensity increases with the significant wave height (Figures 5b and 5c). As more energy is dissipated by depth-induced breaking when the significant wave height increases, it further suggests that non-conservative breaking wave force strengthens locally this seaward-oriented current.

5. Discussion

The results clearly show that the wave-induced circulation plays a crucial role on the cross-shore flow. Circulation patterns show a strong seaward-directed current in the lower part of the water column as far as 4 km from the shoreline, which cannot be reproduced by solely accounting for the wind and the tidal forcing. This unsteady cross-shore circulation is quite well reproduced by the model, which shows excellent predictive skills for short waves with errors on bulk parameters ranging from 4% to 9%. Switching off the wind does not significantly impact the results on short waves because the local wave growth remains weak (not shown). A new configuration

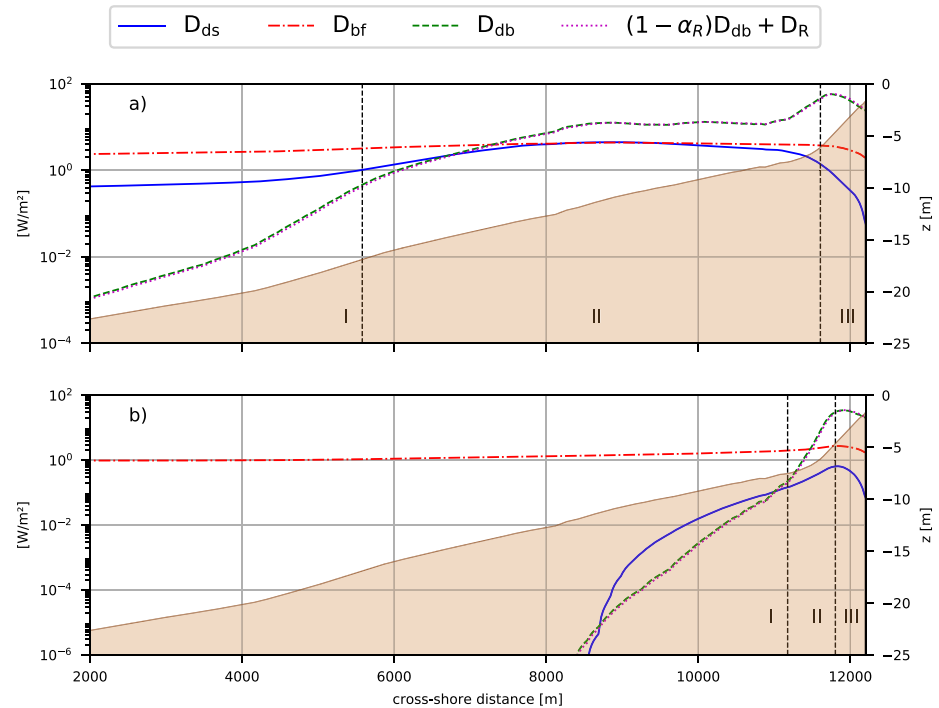


Figure 6. Wave energy dissipation rates profiles associated with bottom friction (D_{bf}), whitecapping (D_{ds}), depth-induced breaking (D_{db}) and roller energy dissipation rates ($(1 - \alpha_R)D_{db} + D_R$) under high (a) or moderate (b) wave energy conditions.

of the model was thus setup with wind and tidal forcing switched off in order to investigate the driving mechanisms of the wave-induced circulation while bypassing the unsteadiness associated with tides and wind. This configuration was run for two distinct 24-hr-periods associated with storm waves ($H_{m0} = 5.3 \text{ m} - 30/01/2021$) and moderate wave energy conditions ($H_{m0} = 2.0 \text{ m} - 04/02/2021$).

5.1. Wave Energy Dissipation Patterns

Considering the significant contribution of the wave energy dissipation processes either on the TKE injection or through the non-conservative wave forces, the energy dissipation rates associated with depth-induced breaking (D_{db}), whitecapping (D_{ds}) and bottom friction (D_{bf}) are first examined following the approach of Pezerat et al. (2021), based on the empirical ratio R reading:

$$R = \frac{D_{db}}{(D_{ds} + D_{bf} + D_{db})} \text{ with } D_x = \int_{\sigma} \int_{\theta} \sigma' S_x d\sigma' d\theta' \quad (15)$$

where the subscript x represents either of the “db”, “ds” or “bf” subscripts. As shown in Figure 6 along a cross-shore profile (see Figure 1), one can distinguish three typical areas. Offshore (zone I, $R < 0.1$), wave energy dissipation is mostly associated with bottom friction. Closer to shore, a transition zone appears (zone II, $0.1 < R < 0.9$), within which bottom friction, whitecapping and depth-induced breaking together significantly contribute to the incident wave energy dissipation, before depth-induced breaking becomes dominant (zone III, $R > 0.9$). Most notably, the transition zone is much wider under high wave energy conditions (approximately 6 km-long spanning from approximately 15 m- to 5 m-depth) than under moderate wave energy conditions (less than 1 km-long with water depth comprised between 5 and 7 m). The edge of the third zone is approximately located at the same distance from the shoreline in both situations ($\approx 5 \text{ m}$ -depth). Interestingly, the wave energy dissipation rates associated with whitecapping and bottom friction are of the same order within the zones I and II under high wave energy conditions, and even dominate the depth-induced breaking contribution over approximately 5 km up to a water-depth of the order of 15 m (Figure 6a). Although it is commonly understood that the surf zone is widening under storm waves, it appears more appropriate to introduce this conceptual transition zone, while the third zone more likely corresponds to the inner surf zone. It is worth noting that the development of this

Table 1
Turbulence Settings for the Runs Rref, Rturb1, Rturb2 and Rturb3

		Mixing length	
		$\alpha_w = 1$	$\alpha_w=0.5$
F_K	$C_{ds} = 1$	Rref	Rturb2
	$C_{ds} = 0$	Rturb1	Rturb3

Note. The mixing length increases with α_w while C_{ds} controls the TKE injection associated with wave energy dissipation through whitecapping.

Table 2
Relative Difference (in %) $RD_{1/2}(X) = |\hat{X}_1 - \hat{X}_2|/|\hat{X}_2|$ of Modeled Turbulent Kinetic Energy (K), Vertical Eddy Viscosity (ν) and Cross-Shore Velocity (\hat{u}) Vertical Profiles for the Different Configurations of the Model Within the Three Delimited Area Introduced in Section 5.1, Under High (HE) or Moderate (LE) Wave Energy Conditions

	Rturb1/Rref	Rturb3/Rturb2	Rturb2/Rref	Rturb3/Rturb1
HE				
zone I				
RD(K)	92	88	30	5
RD(ν)	62	49	42	8
RD(\hat{u})	3	6	12	4
zone II				
RD(K)	60	56	27	21
RD(ν)	25	23	41	28
RD(\hat{u})	7	4	28	19
zone III				
RD(K)	2	2	16	16
RD(ν)	<1	<1	29	29
RD(\hat{u})	<1	<1	30	30
LE				
zone I				
RD(K)	66	60	25	12
RD(ν)	26	18	26	12
RD(\hat{u})	2	2	10	7
zone II				
RD(K)	30	28	24	21
RD(ν)	10	9	29	25
RD(\hat{u})	2	2	32	27
zone III				
RD(K)	4	3	16	16
RD(ν)	<1	<1	29	29
RD(\hat{u})	<1	<1	30	30

Note. High RD values indicate a strong sensitivity to turbulence settings, either to the mixing length or the surface flux of TKE.

wide transition zone is also presumably related to the gentle and smoothly increasing bottom slope that characterizes the study area, while the transition to a regime dominated by depth-induced breaking is much more abrupt over barred beach or fringing environments. It would be thus interesting to perform similar analysis in contrasted environments, with a diversity of beach profiles and bottom substrate.

The roller model shows a weak effect on the location where energy is dissipated. This could be presumably attributed to the gentle bottom slope characterizing the study area, while previous studies highlighted the significant roller effect over a barred and steeper beach (e.g., Kumar et al., 2012; Reniers et al., 2004; Uchiyama et al., 2010; Zheng et al., 2017).

5.2. Sensitivity to Vertical Mixing

The results presented above show a substantial wave energy dissipation associated with whitecapping and depth-induced breaking as far as 6 km from the shoreline under energetic conditions, which further suggest that a substantial amount of TKE could be injected at the surface. Three principal parameters control the injection of TKE at the surface (C_{db} and C_{ds}) and its vertical decay (z_0^s). If we consider the default value taken for C_{db} and C_{ds} , we note that for equivalent energy dissipated through whitecapping and depth-induced breaking (i.e., $D_{ds} \sim D_{db}$), more weight is given to the whitecapping contribution. Previous studies have highlighted the effect of breaking-wave-generated turbulence on the mean circulation within the surf zone, which results in a reduction of the vertical shear of the horizontal current (e.g., Feddersen & Trowbridge, 2005; Kumar et al., 2012). In intermediate water depths, Paskyabi et al. (2012) showed that surface currents associated with Ekman transport are better reproduced when accounting for whitecapping contribution to the wave-enhanced mixing, while Lentz et al. (2008) used a crude parameterization based on the wind stress for the vertical eddy viscosity for their study over the inner continental shelf. Overall, the contribution of the wave-enhanced turbulence to the mean circulation under the combined effects of depth-induced breaking and whitecapping has thus never been evaluated across the shoreface (note that Kumar et al., 2012, gathered both contributions to compute the surface flux of TKE and used $C_{db} = C_{ds}$). In addition, a sensitivity analysis of the vertical shear of the mean cross-shore current to the parameterization of the surface mixing length z_0^s was performed to supplement the study of Moghimi et al. (2016), who highlighted the sensitivity of turbulence closure models to z_0^s because of the power law for the decay of the TKE. Three additional runs were thus retained (see Table 1) to assess the sensitivity of the vertical mixing to the parameterization of the TKE injection and how it further impacts the cross-shore circulation. The results are compared along vertical profiles of TKE (K), vertical eddy viscosity (ν) and cross-shore quasi-Eulerian velocity component (\hat{u}) distributed along the aforementioned cross-shore profile (see Figure 7 and Table 2).

Under storm conditions, whitecapping explains more than two-third of the TKE injected at the surface in regions I and II. This greatly affects the mixing in the upper third of the water column (see ν almost doubled at some locations between Rref and Rturb1 in Figure 7). Note, however, that it only slightly impacts the cross-shore circulation ($RD(\hat{u}) \leq 7\%$, see the comparisons Rturb1/Rref and Rturb3/Rturb2 in Table 2), with the largest differences being found in the upper part of the water column. Furthermore, in both high or moderate wave energy conditions, the model shows a strong sensitivity

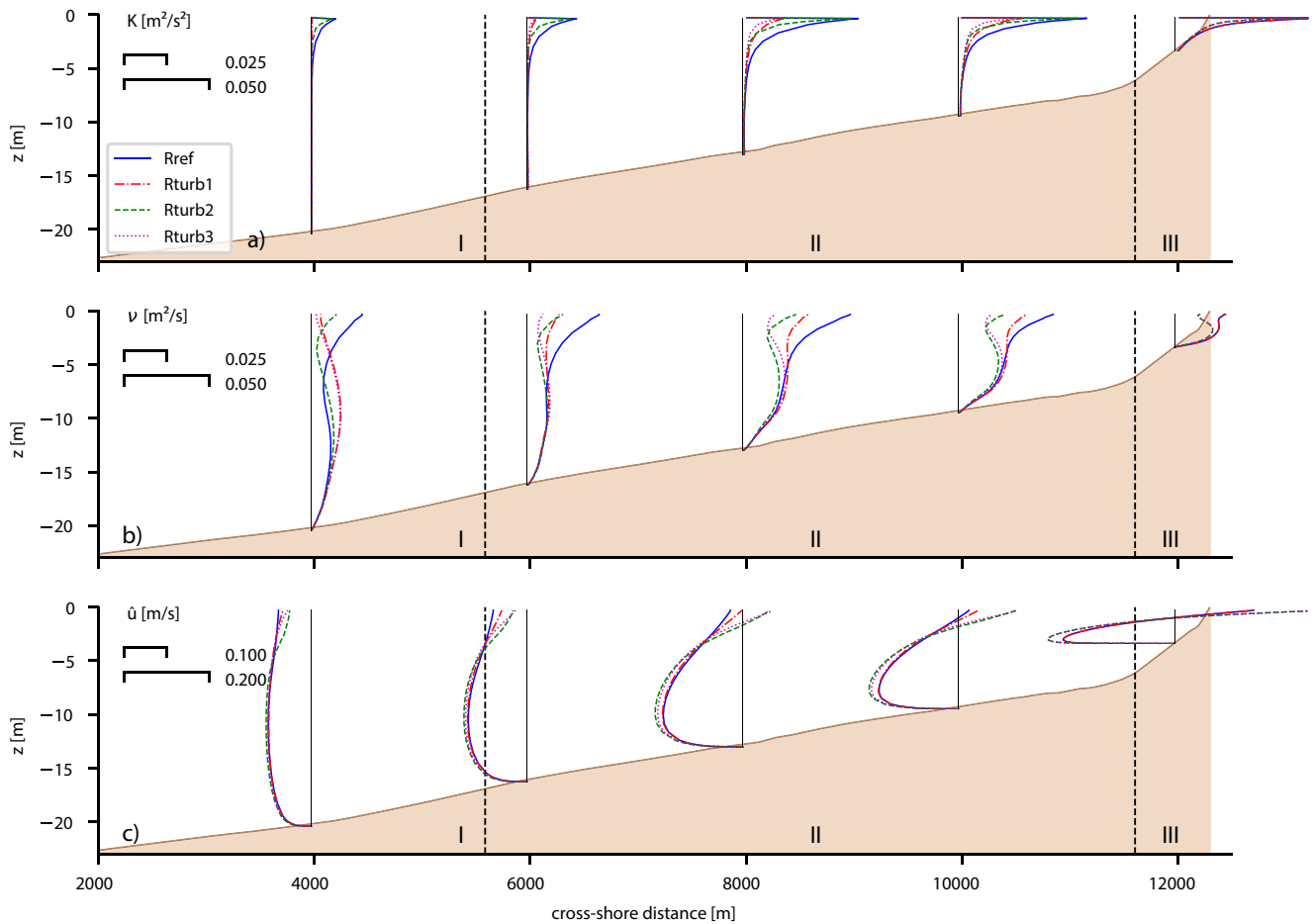


Figure 7. Vertical profiles of turbulent kinetic energy (K , panel a), vertical eddy viscosity (ν , panel b) and quasi-Eulerian cross-shore velocity (\hat{u} , panel c). The results are presented for the four configurations of the model (see Table 1) and are extracted under high wave energy conditions. The delimited zones are defined in Section 5.1.

to the parameterization of the surface mixing length, which strengthens as the injection of TKE at the surface increases closer to shore (within the zones II and III, see Table 2). With a shorter surface mixing length, the eddy viscosity at the surface is weaker, such that the cross-shore velocity profiles are more sheared (see Figure 7 under high wave energy conditions, while similar results – not shown – are found under moderate wave energy conditions). As a result, the orientation of the cross-shore flow near the surface even changes for one profile within the zone II under high energy condition with a shorter mixing length. The relative difference on the cross-shore velocity reaches 32% depending on the parameterization of z_0^* . Interestingly, comparing R_{turb2}/R_{ref} and R_{turb3}/R_{turb1} tends to show that the sensitivity to the parameterization of the surface mixing length is stronger depending on the contribution of the whitcapping to the TKE injection (see Table 2). Overall, it appears that the parameterization of the TKE injection impacts the vertical shear of the cross-shore velocity as far as 6 km from the shoreline under energetic conditions.

5.3. Wave-Induced Circulation Patterns and Forcing Mechanisms

Under moderate wave energy conditions, non-conservative breaking wave forces arise relatively close to shore, up to 1 km from the shoreline (Figure 8a) and are mostly associated with depth-induced breaking, which dominates the wave energy dissipation within the zones II and III (Figure 6b). The quasi-Eulerian cross-shore flow therefore shows a strong seaward-directed current reaching 0.3 m/s in the lower part of the water column, whereas a shoreward-directed current arises near the surface (Figure 8c). The depth-averaged quasi-Eulerian cross-shore flow (i.e., the undertow) nearly compensates for the depth-averaged cross-shore Stokes drift velocity component

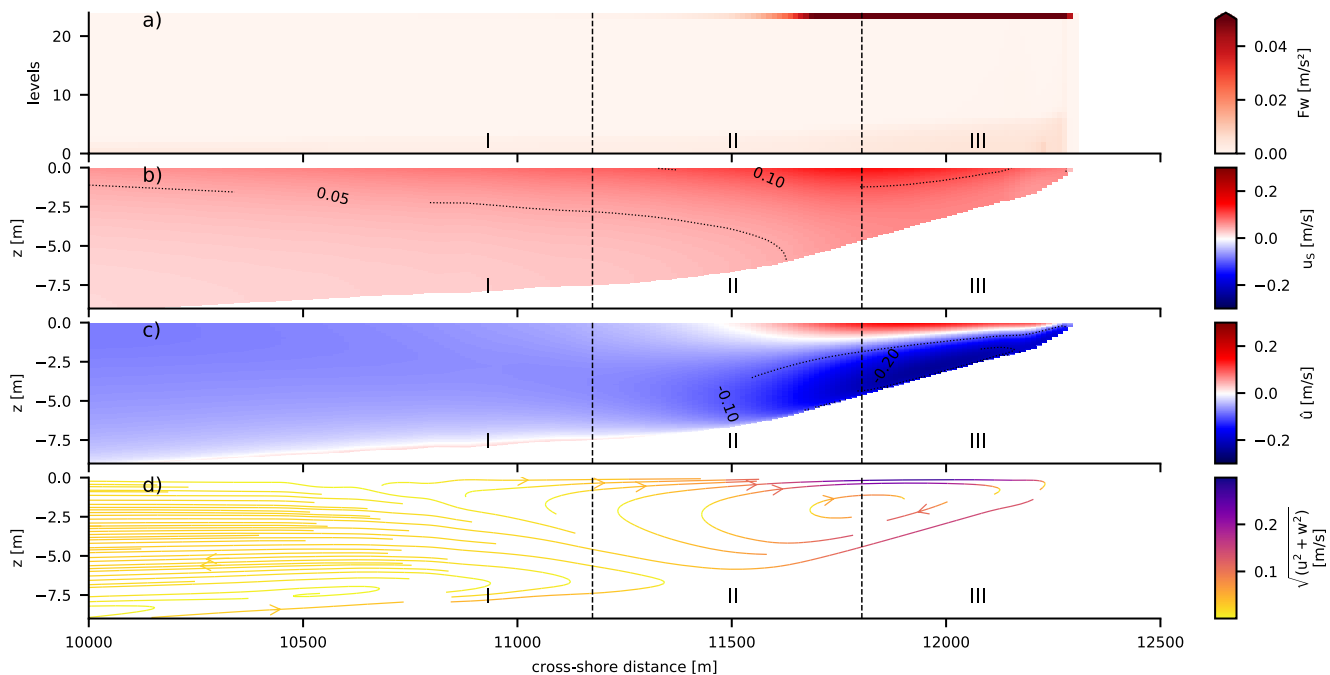


Figure 8. Cross-shore profiles under moderate wave energy conditions of the wave force cross-shore component, which includes the Stokes-Coriolis term, the vortex force, the wave-induced pressure term and the non-conservative wave forces (a), the Stokes drift velocity cross-shore component (b), the quasi-Eulerian velocity cross-shore component (c), and the 2DV Lagrangian circulation streamlines and magnitude (d). For readability, S-level indices are used for representing the wave force profile (the level 0 corresponds to the bottom and the level 24 to the free surface). Note that the cross-shore distance axis here extends over 2 km.

(the divergence of the alongshore velocity component is not exactly zero), while the depth-varying cross-shore flow is locally strengthened by the effect of the non-conservative breaking wave forces within the zones II and III, resulting in a 100% stronger seaward-directed current in the lower part of the water column than the surface Stokes drift velocity (Figures 8b and 8c and 10b). In order to better evaluate the contribution of breaking, an additional run was performed with the non-conservative breaking wave forces uniformly distributed over the vertical (RF_{br}). The resulting quasi-Eulerian cross-shore flow is less sheared near the surface within the zones II and III, yielding a weaker seaward-directed current in the lower part of the water column than that obtained with a near surface momentum source by up to a factor three (Figure 10b). Within zone I, the quasi-Eulerian cross-shore flow is also mostly seaward-directed, with a maximum intensity in the upper part of the water column, while a weak shoreward-directed current associated with wave streaming arises near the bottom and extends inside the zone II (Figures 8a and 8c and 10b). As a result, a strong clockwise Lagrangian overturning circulation develops within the zones II and III (the magnitude of the current locally reaches 0.3 m/s), while a weaker anti-clockwise overturning cell arises at the seaward edge of the zone II, which constrains the offshore flow (see the upward deflection of the streamlines of the clockwise cell within the zone II in Figure 8d). A similar circulation pattern in the vicinity of the surf zone was found by Wang et al. (2020). The magnitude of the Lagrangian circulation then decreases relatively rapidly within zone I (Figure 8d). Interestingly, the cross-shore quasi-Eulerian flow does not exactly compensate for the cross-shore Stokes drift velocity component, which would have been expected assuming a balance between the Coriolis force associated with the quasi-Eulerian flow and the Stokes-Coriolis force, as pointed out by Lentz et al. (2008). Presumably, this could be attributed to the shape of the coastline, which is not alongshore-uniform at the scale of several kilometers, the distance where the instruments were located.

Under high wave energy conditions, non-conservative breaking wave forces arise at the surface as far as 6 km from the shoreline and strengthen shoreward (Figure 9a), associated with a significant wave energy dissipation occurring through whitecapping and depth-induced breaking within the zones II and III (Figure 6a). The quasi-Eulerian cross-shore flow shows a strong seaward-directed current of the order of 0.2 m/s up to 4 km from the shoreline, whose intensity progressively decreases offshore reaching 0.1 m/s as far as 10 km from the shoreline (Figure 9c). Similar to moderate wave energy conditions, this current is strengthened locally by the effect of the non-conservative breaking wave forces within the zones II and III (Figure 10a). Interestingly, no near-bottom

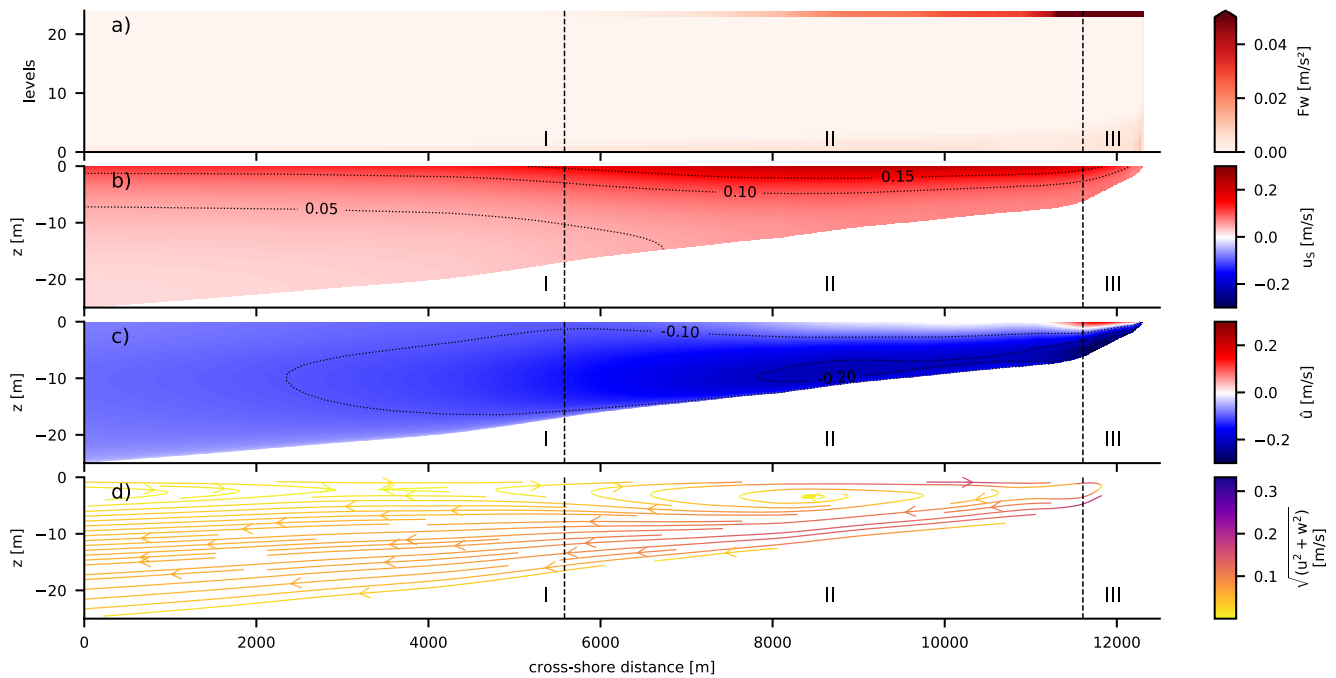


Figure 9. Same as Figure 8 under high wave energy conditions. Note that the cross-shore distance axis here extends over 12 km.

shoreward-directed current arises as the intensity of the bottom streaming decreases beyond 20 m-depth, while closer to shore the cross-shore flow in the lower part of the water column is dominated by the strong seaward-directed current. The Lagrangian circulation therefore shows a wide clockwise overturning cell extending over 8 km, which generates a seaward-oriented jet in the lower part of the water column (Figure 9d) that contrasts with the circulation pattern obtained under moderate wave energy conditions.

6. Conclusions and Perspectives

In this study, we presented a data set comprising water levels, wave parameters and currents collected under fair weather and storm conditions issued from a field campaign carried out in early 2021 within the shoreface and the surf zone of the dissipative beach of Saint-Trojan (France). These results were complemented with the predictions from a state-of-the-art wave-averaged 3D circulation modeling system coupling the circulation model SCHISM (Zhang et al., 2016) with the spectral wave model WWM (Roland et al., 2012) in order to study the wave-induced cross-shore circulation in the nearshore area up to the surf zone. Both measurements and model results clearly showed that the cross-shore flow is dominated by a strong seaward-directed current in the lower part of the water column, which under storm wave conditions can reach 0.2 m/s as far as 4 km from the shoreline. The model was further employed to study the driving mechanisms of the wave-induced cross-shore circulation. It was shown that a wide (≈ 6 km) transition zone appears under high wave energy conditions where depth-induced breaking, whitecapping and bottom friction all contribute significantly to the wave energy dissipation, whereas the surf zone edge appears clearly delimited under moderate wave energy conditions. Once wave energy dissipation through breaking processes starts being substantial, sensitivity tests performed with the model tended to show that the parameterization of the wave-enhanced mixing could substantially impact the vertical shear of the cross-shore velocity close to the surface, while non-conservative breaking wave forces strengthen locally the seaward-directed current in the lower part of the water column. The wave-induced cross-shore circulation thus presents very contrasting patterns. Under moderate wave energy conditions, the dominance of the wave energy dissipation by bottom friction seaward of the surf zone allows the development of a near-bottom onshore flow associated with bottom streaming of the order of a few centimeters per second. Thus, the surf zone clockwise Lagrangian overturning circulation weakens, while an additional anti-clockwise overturning cell arises seaward of the surf zone and extends within it. In contrast, under high energy conditions the Lagrangian circulation shows a seaward-directed jet in the lower part of the water column, whose intensity progressively decreases offshore.

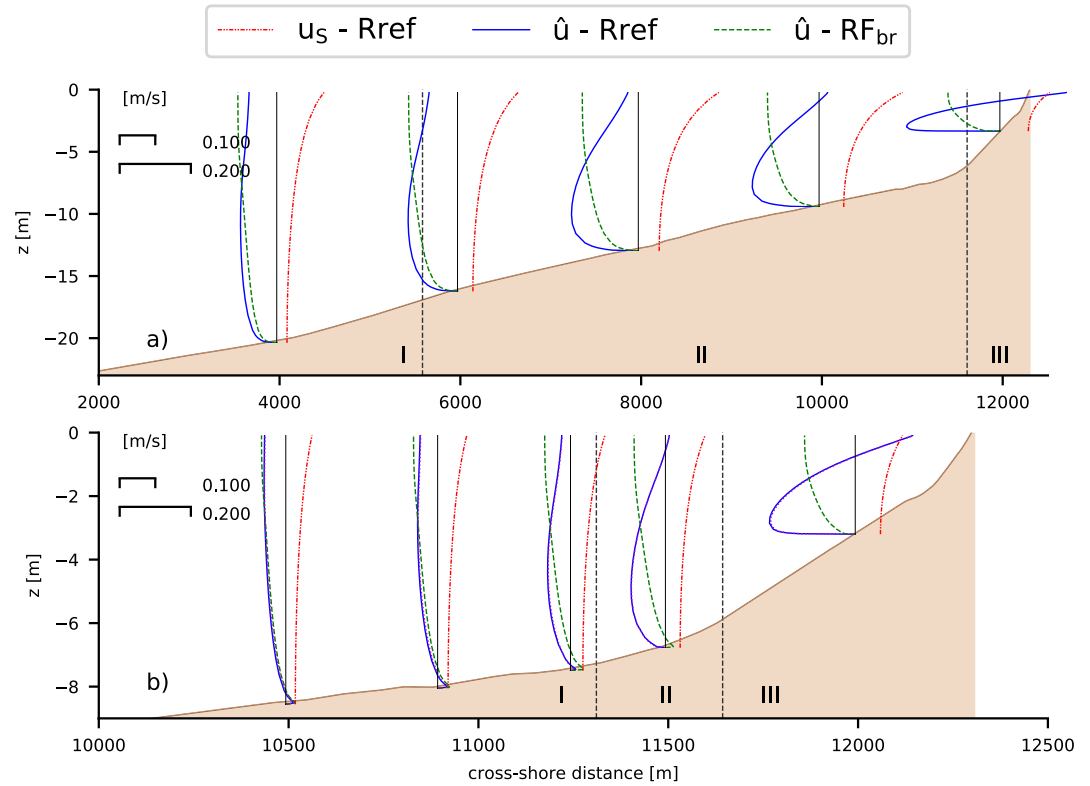


Figure 10. Vertical profiles of the Stokes drift velocity cross-shore component (u_S) and the quasi-Eulerian cross-shore velocity (\hat{u}) under high (a) or moderate (b) wave energy conditions for the baseline run (Rref) and for a run performed with the non-conservative breaking wave forces uniformly distributed (RF_{br}). The delimited zones are defined in Section 5.1.

Among different implications, this study opens perspectives for sediment transport modeling using a similar 3D framework in order to produce realistic morphological evolutions across the shoreface.

Appendix A: Vortex Force Framework in the Modeling System SCHISM

In the vortex force framework the continuity and momentum equations read:

$$\frac{\partial \hat{u}}{\partial x} + \frac{\partial \hat{v}}{\partial y} + \frac{\partial \hat{w}}{\partial z} = 0 \quad (\text{A1})$$

$$\frac{D\hat{u}}{Dt} - f\hat{v} = -\frac{1}{\rho} \frac{\partial P_H}{\partial x} + \frac{\partial}{\partial z} \left(\nu \frac{\partial \hat{u}}{\partial z} \right) + v_S \left(f_C + \left(\frac{\partial \hat{v}}{\partial x} - \frac{\partial \hat{u}}{\partial y} \right) \right) - w_S \frac{\partial \hat{u}}{\partial z} - \frac{\partial J}{\partial x} + \hat{F}_x \quad (\text{A2})$$

$$\frac{D\hat{v}}{Dt} + f\hat{u} = -\frac{1}{\rho} \frac{\partial P_H}{\partial y} + \frac{\partial}{\partial z} \left(\nu \frac{\partial \hat{v}}{\partial z} \right) - u_S \left(f_C + \left(\frac{\partial \hat{v}}{\partial x} - \frac{\partial \hat{u}}{\partial y} \right) \right) - w_S \frac{\partial \hat{v}}{\partial z} - \frac{\partial J}{\partial y} + \hat{F}_y \quad (\text{A3})$$

where $[\hat{u}, \hat{v}, \hat{w}]$ is the quasi-Eulerian velocity, equal to the mean Lagrangian velocity $[u, v, w]$ minus the Stokes drift velocity $[u_S, v_S, w_S]$. In Equations A2 and A3, f_C is the Coriolis parameter, ρ is the water density, g is the gravitational acceleration, ν is the vertical eddy viscosity, P_H is the hydrostatic pressure, J is the wave-induced mean pressure and $[\hat{F}_x, \hat{F}_y]$ gathers the non-conservative wave forces.

The three components of the Stokes drift velocities, the wave-induced pressure term and the non-conservative wave forces are all computed from local variables issued from WWM, which simulates the generation, propagation and transformation of short waves by solving the Wave Action Equation (e.g., Komen et al., 1994):

$$\frac{\partial N}{\partial t} + \frac{\partial}{\partial x} ((C_{g,x} + \bar{u}) N) + \frac{\partial}{\partial y} ((C_{g,y} + \bar{v}) N) + \frac{\partial (\hat{\sigma} N)}{\partial \sigma} + \frac{\partial (\hat{\theta} N)}{\partial \theta} = S_{tot} \quad (\text{A4})$$

where σ is the relative wave frequency, which is related to the wavenumber k by the linear dispersion relation; θ corresponds to the wave direction; $N = \rho g E / \sigma$ is the wave action density spectrum, with E the sea surface elevation density spectrum; $[C_{g,x}, C_{g,y}]$ is the intrinsic group velocity; $[\bar{u}, \bar{v}]$ is the advective current velocity, here equal to the depth-averaged horizontal quasi-Eulerian velocity. Finally, S_{tot} is a sum of source terms that account for the energy input due to wind, non linear wave-wave interactions, and energy dissipation due to whitecapping, depth-induced breaking and bottom friction (cf., Section 3.1).

The horizontal Stokes drift velocity vector is given by:

$$[u_S, v_S] = \int_{\sigma} \int_{\theta} \sigma' k E \frac{\cosh(2k(z+d))}{\sinh^2(kh)} [\cos\theta', \sin\theta'] d\sigma' d\theta' \quad (\text{A5})$$

where $h = d + \bar{\eta}$ is the (local) phase-averaged water depth (with d , the still water depth and $\bar{\eta}$, the phase-averaged free surface elevation). The vertical Stokes drift component is given by the horizontal divergence of $[u_S, v_S]$ as the full Stokes drift flow is non divergent at the lowest order (Ardhuin et al., 2008). The wave-induced pressure term reads:

$$J = \int_{\sigma} \int_{\theta} \frac{gkE}{\sinh(2kh)} d\sigma' d\theta' \quad (\text{A6})$$

Finally, the formulation of the non-conservative wave forces are detailed in Section 3.2.1.

The wave model is supplemented by a roller model that helps representing the inertia of depth-induced breaking processes by slightly advecting the location where energy is actually dissipated toward the shoreline (Svendensen, 1984b). As compared to the implementation detailed in Gu erin et al. (2018), the roller model solves a balance equation for the roller kinetic energy E_R (e.g., Reniers et al., 2004), slightly modified to account for the modification of the wave phase velocity by the mean current within the advection term, such that:

$$\frac{\partial E_R}{\partial t} + \frac{\partial}{\partial x} (2E_R (c_x + \bar{u})) + \frac{\partial}{\partial y} (2E_R (c_y + \bar{v})) = \alpha_R D_{db} - D_R \quad (\text{A7})$$

where $[c_x, c_y]$ is the wave phase velocity computed by means of the short wave (continuous) peak wavenumber (k_p) and mean direction (θ_m); D_{db} is the bulk wave energy dissipation rate by depth-induced breaking; α_R is the percentage of wave energy dissipation by depth-induced breaking transferred to the rollers (Tajima & Madsen, 2006) and D_R is the roller energy dissipation rate, which reads:

$$D_R = \frac{2g \sin\beta_R E_R}{\sqrt{c_x^2 + c_y^2}} \quad (\text{A8})$$

where $\sin\beta_R = 0.1$ is the roller angle (Nairn et al., 1991; Reniers et al., 2004). Surface rollers contribute to the total mass flux in proportion to the roller energy. Although this transport primarily occurs near the surface, above trough level, there is no consensus on its vertical distribution. We here follow the choice to impose an homogeneous vertical distribution. This contribution is accounted for through an additional term in the horizontal Stokes drift velocity vector, which reads:

$$[u_{S,R}, v_{S,R}] = \frac{2E_R}{\rho h \sqrt{c_x^2 + c_y^2}} [\cos\theta_m, \sin\theta_m] \quad \forall z \in [-d, \bar{\eta}] \quad (\text{A9})$$

Note, however, that w_S is still computed with u_S, v_S from Equation A5 as it is assumed that rollers do not contribute to the vertical transport.

Data Availability Statement

The processed field data presented in this study are available through a Zenodo repository (Pezerat et al., 2022). The instructions to download and install the model used in this study can be accessed freely at <https://github.com/schism-dev/schism>. Figures were made with python module Matplotlib version 3.1.1, available under the Matplotlib licenses at <https://matplotlib.org/>.

Acknowledgments

M. Pezerat is supported by a PhD fellowship from CDA La Rochelle and from the FEDER project DURALIT. K. Martins greatly acknowledges the financial support from the University of Bordeaux, through an International Postdoctoral Grant (I dex, nb. 1024R-5030). L. Lavaud is supported by a PhD fellowship from the Region Nouvelle-Aquitaine and the UNIMA engineering consulting company. The authors appreciate the administrative support of the DDTM to carry out long term deployment of sensors. The topo-bathymetric data of the studied area were acquired in the scope of the National Observation System DYNALIT (<https://www.dynalit.fr>), part of the research infrastructure ILICO. The Observatoire de la Côte Aquitaine (OCA) partly funded the field campaign presented in this study. Model development carried out in this study is a contribution to the project "Segundo Torrao", funded by the Fondation de France and Fondation Edouard et Geneviève Buffard through the program "Nouveaux commanditaires Science". N. Lachaussée built the structures to anchor the sensors, whereas T. Coulombier and D. Dausse provided valuable assistance during the field campaign. Lastly, the authors want to thank O. de Viron for his enlightening insights on data post-processing, and the two anonymous reviewers for their constructive comments.

References

Abdolali, A., Roland, A., Van Der Westhuysen, A., Meixner, J., Chawla, A., Hesser, T. J., et al. (2020). Large-scale hurricane modeling using domain decomposition parallelization and implicit scheme implemented in wavewatch iii wave model. *Coastal Engineering*, *157*, 103656. <https://doi.org/10.1016/j.coastaleng.2020.103656>

Appell, G. F., Bass, P., & Metcalf, M. A. (1991). Acoustic doppler current profiler performance in near surface and bottom boundaries. *IEEE Journal of Oceanic Engineering*, *16*(4), 390–396. <https://doi.org/10.1109/48.90903>

Ardhuin, F., O'Reilly, W. C., Herbers, T. H. C., & Jessen, P. F. (2003). Swell transformation across the continental shelf. Part I: Attenuation and directional broadening. *Journal of Physical Oceanography*, *33*, 1921–1939. [https://doi.org/10.1175/1520-0485\(2003\)033<1921:statcs>2.0.co;2](https://doi.org/10.1175/1520-0485(2003)033<1921:statcs>2.0.co;2)

Ardhuin, F., Rasclé, N., & Belibassakis, K. A. (2008). Explicit wave-averaged primitive equations using a generalized lagrangian mean. *Ocean Modelling*, *20*(1), 35–60. <https://doi.org/10.1016/j.ocemod.2007.07.001>

Ardhuin, F., Rogers, E., Babanin, A. V., Filipot, J.-F., Magne, R., Roland, A., et al. (2010). Semiempirical dissipation source functions for ocean waves. Part I: Definition, calibration, and validation. *Journal of Physical Oceanography*, *40*(9), 1917–1941. <https://doi.org/10.1175/2010jpo4324.1>

Battjes, J. A., & Janssen, J. (1978). Energy loss and set-up due to breaking of random waves. *Coastal Engineering*, *569*–587. <https://doi.org/10.1061/9780872621909.034>

Battjes, J. A., & Stive, M. (1985). Calibration and verification of a dissipation model for random breaking waves. *Journal of Geophysical Research*, *90*(C5), 9159–9167. <https://doi.org/10.1029/jc090ic05p09159>

Bennis, A.-C., Ardhuin, F., & Dumas, F. (2011). On the coupling of wave and three-dimensional circulation models: Choice of theoretical framework, practical implementation and adiabatic tests. *Ocean Modelling*, *40*(3–4), 260–272. <https://doi.org/10.1016/j.ocemod.2011.09.003>

Bertin, X., Bruneau, N., Breilh, J.-F., Fortunato, A. B., & Karpytchev, M. (2012). Importance of wave age and resonance in storm surges: The case xynthia, Bay of Biscay. *Ocean Modelling*, *42*, 16–30. <https://doi.org/10.1016/j.ocemod.2011.11.001>

Bertin, X., Castelle, B., Chaumillon, E., Butel, R., & Quique, R. (2008). Longshore transport estimation and inter-annual variability at a high-energy dissipative beach: St. Trojan beach, SW Oléron Island, France. *Continental Shelf Research*, *28*(10–11), 1316–1332. <https://doi.org/10.1016/j.csr.2008.03.005>

Bertin, X., Li, K., Roland, A., & Bidlot, J.-R. (2015). The contribution of short-waves in storm surges: Two case studies in the bay of Biscay. *Continental Shelf Research*, *96*, 1–15. <https://doi.org/10.1016/j.csr.2015.01.005>

Bertin, X., Martins, K., de Bakker, A., Chataigner, T., Guérin, T., Coulombier, T., & de Viron, O. (2020). Energy transfers and reflection of infragravity waves at a dissipative beach under storm waves. *Journal of Geophysical Research: Oceans*, *125*(5), e2019JC015714. <https://doi.org/10.1029/2019jc015714>

Bishop, C. T., & Donelan, M. A. (1987). Measuring waves with pressure transducers. *Coastal Engineering*, *11*(4), 309–328. [https://doi.org/10.1016/0378-3839\(87\)90031-7](https://doi.org/10.1016/0378-3839(87)90031-7)

Blumberg, A. F., & Mellor, G. L. (1987). A description of a three-dimensional coastal ocean circulation model. *Three-dimensional coastal ocean models*, *4*, 1–16. <https://doi.org/10.1029/co004p0001>

Booij, N., Ris, R. C., & Holthuijsen, L. H. (1999). A third-generation wave model for coastal regions: 1. Model description and validation. *Journal of geophysical research*, *104*(C4), 7649–7666. <https://doi.org/10.1029/98jc02622>

Burchard, H., Bolding, K., & Villarreal, M. (1999). *Gotm, a general ocean turbulence model: Theory, implementation and test cases* (Tech. Rep. No. EUR18745). European Commission.

Castelle, B., Mariou, V., Bujan, S., Splinter, K. D., Robinet, A., Sénéchal, N., & Ferreira, S. (2015). Impact of the winter 2013–2014 series of severe western Europe storms on a double-barred sandy coast: Beach and dune erosion and megacusp embayments. *Geomorphology*, *238*, 135–148. <https://doi.org/10.1016/j.geomorph.2015.03.006>

Coco, G., Senechal, N., Rejas, A., Bryan, K. R., Capo, S., Parisot, J., et al. (2014). Beach response to a sequence of extreme storms. *Geomorphology*, *204*, 493–501. <https://doi.org/10.1016/j.geomorph.2013.08.028>

Craig, P. D., & Banner, M. L. (1994). Modeling wave-enhanced turbulence in the ocean surface layer. *Journal of Physical Oceanography*, *24*(12), 2546–2559. [https://doi.org/10.1175/1520-0485\(1994\)024<2546:mwetit>2.0.co;2](https://doi.org/10.1175/1520-0485(1994)024<2546:mwetit>2.0.co;2)

De Bakker, A., Herbers, T., Smit, P., Tissier, M., & Ruessink, B. (2015). Nonlinear infragravity–wave interactions on a gently sloping laboratory beach. *Journal of Physical Oceanography*, *45*(2), 589–605. <https://doi.org/10.1175/jpo-d-14-0186.1>

Deigaard, R., Justesen, P., & Fredsøe, J. (1991). Modelling of undertow by a one-equation turbulence model. *Coastal Engineering*, *15*(5–6), 431–458. [https://doi.org/10.1016/0378-3839\(91\)90022-9](https://doi.org/10.1016/0378-3839(91)90022-9)

Delpy, M., Ardhuin, F., Otheguy, P., & Jouan, A. (2014). Effects of waves on coastal water dispersion in a small estuarine bay. *Journal of Geophysical Research: Oceans*, *119*(1), 70–86. <https://doi.org/10.1002/2013jc009466>

Déqué, M., Dreveton, C., Braun, A., & Cariolle, D. (1994). The arpege/ifs atmosphere model: A contribution to the French community climate modelling. *Climate Dynamics*, *10*(4), 249–266. <https://doi.org/10.1007/bf00208992>

Dodet, G., Bertin, X., Bouchette, F., Gravelle, M., Testut, L., & Wöppelmann, G. (2019). Characterization of sea-level variations along the metropolitan coasts of France: Waves, tides, storm surges and long-term changes. *Journal of Coastal Research*, *88*, 10–24. <https://doi.org/10.2112/si88-003.1>

Eldeberky, Y. (1997). Nonlinear transformation of wave spectra in the nearshore zone. *Oceanographic Literature Review*, *4*(44), 297.

Eldeberky, Y., & Battjes, J. A. (1996). Spectral modeling of wave breaking: Application to boussinesq equations. *Journal of Geophysical Research*, *101*(C1), 1253–1264. <https://doi.org/10.1029/95jc03219>

Elgar, S., & Raubenheimer, B. (2020). Field evidence of inverse energy cascades in the surfzone. *Journal of Physical Oceanography*, *50*(8), 2315–2321. <https://doi.org/10.1175/jpo-d-19-0327.1>

Fedderson, F. (2012a). Observations of the surf-zone turbulent dissipation rate. *Journal of Physical Oceanography*, *42*(3), 386–399. <https://doi.org/10.1175/jpo-d-11-082.1>

Fedderson, F. (2012b). Scaling surf zone turbulence. *Geophysical Research Letters*, *39*(18). <https://doi.org/10.1029/2012gl052970>

Fedderson, F. (2014). The generation of surfzone eddies in a strong alongshore current. *Journal of Physical Oceanography*, *44*(2), 600–617. <https://doi.org/10.1175/jpo-d-13-051.1>

Fedderson, F., & Trowbridge, J. (2005). The effect of wave breaking on surf-zone turbulence and alongshore currents: A modeling study. *Journal of Physical Oceanography*, *35*(11), 2187–2203. <https://doi.org/10.1175/jpo2800.1>

Garcez Faria, A., Thornton, E., Lippmann, T., & Stanton, T. (2000). Undertow over a barred beach. *Journal of Geophysical Research*, *105*(C7), 16999–17010. <https://doi.org/10.1029/2000jc900084>

- Goring, D. G., & Nikora, V. I. (2002). Despiking acoustic doppler velocimeter data. *Journal of Hydraulic Engineering*, 128(1), 117–126. [https://doi.org/10.1061/\(asce\)0733-9429\(2002\)128:1\(117\)](https://doi.org/10.1061/(asce)0733-9429(2002)128:1(117))
- Grant, W. D., & Madsen, O. S. (1982). Movable bed roughness in unsteady oscillatory flow. *Journal of Geophysical Research*, 87, 469–481. <https://doi.org/10.1029/jc087ic01p00469>
- Guérin, T., Bertin, X., Coulombier, T., & de Bakker, A. (2018). Impacts of wave-induced circulation in the surf zone on wave setup. *Ocean Modelling*, 123, 86–97. <https://doi.org/10.1016/j.ocemod.2018.01.006>
- Haines, J. W., & Sallenger, A. H., Jr. (1994). Vertical structure of mean cross-shore currents across a barred surf zone. *Journal of Geophysical Research*, 99(C7), 14223–14242. <https://doi.org/10.1029/94jc00427>
- Hamm, L., & Peronnard, C. (1997). Wave parameters in the nearshore: A clarification. *Coastal Engineering*, 32(2–3), 119–135. [https://doi.org/10.1016/s0378-3839\(97\)81746-2](https://doi.org/10.1016/s0378-3839(97)81746-2)
- Hasselmann, K. (1970). Wave-driven inertial oscillations. *Geophysical and Astrophysical Fluid Dynamics*, 1(3–4), 463–502. <https://doi.org/10.1080/03091927009365783>
- Hasselmann, S., Hasselmann, K., Allender, J., & Barnett, T. (1985). Computations and parameterizations of the nonlinear energy transfer in a gravity-wave spectrum. Part II: Parameterizations of the nonlinear energy transfer for application in wave models. *Journal of Physical Oceanography*, 15(11), 1378–1391. [https://doi.org/10.1175/1520-0485\(1985\)015<1378:capotn>2.0.co;2](https://doi.org/10.1175/1520-0485(1985)015<1378:capotn>2.0.co;2)
- Huang, Z.-C., Hsiao, S.-C., Hwung, H.-H., & Chang, K.-A. (2009). Turbulence and energy dissipations of surf-zone spilling breakers. *Coastal Engineering*, 56(7), 733–746. <https://doi.org/10.1016/j.coastaleng.2009.02.003>
- Klopman, G. (1994). *Vertical structure of the flow due to waves and currents – Laser-doppler flow measurements for waves following or opposing a current* (Technical Report No., H840–30). Deltares (WL).
- Komen, G. J., Cavaleri, L., Donelan, M., Hasselmann, K., Hasselmann, S., & Janssen, P. A. E. M. (1994). *Dynamics and modelling of ocean waves*. Cambridge, U.K: Cambridge University Press. <https://doi.org/10.1017/CBO9780511628955>
- Kumar, N., Voulgaris, G., Warner, J. C., & Olabarrieta, M. (2012). Implementation of the vortex force formalism in the coupled ocean-atmosphere-wave-sediment transport (coast) modeling system for inner shelf and surf zone applications. *Ocean Modelling*, 47, 65–95. <https://doi.org/10.1016/j.ocemod.2012.01.003>
- Lavaud, L., Pezerat, M., Coulombier, T., Bertin, X., & Martins, K. (2020). Hydrodynamics on a rocky shore under moderate-energy wave conditions. *Journal of Coastal Research*, 95, 1473–1479. <https://doi.org/10.2112/si95-284.1>
- Lentz, S. J., Fewings, M., Howd, P., Fredericks, J., & Hathaway, K. (2008). Observations and a model of undertow over the inner continental shelf. *Journal of Physical Oceanography*, 38(11), 2341–2357. <https://doi.org/10.1175/2008jpo3986.1>
- Long, J. W., & Özkan-Haller, H. T. (2009). Low-frequency characteristics of wave group–forced vortices. *Journal of Geophysical Research*, 114(C8). <https://doi.org/10.1029/2008jc004894>
- Longuet-Higgins, M. (1953). Mass transport in water waves. *Philosophical Transactions of the Royal Society*, 245, 535–581.
- Madsen, O. S. (1995). Spectral wave-current bottom boundary layer flows. *Coastal Engineering*, 1994, 384–398. <https://doi.org/10.1061/9780784400890.030>
- Madsen, O. S., Poon, Y. K., & Graber, H. C. (1988). Spectral wave attenuation by bottom friction: Theory. In *21st international conference on coastal engineering* (pp. 492–504). Malaga: ASCE. <https://doi.org/10.9753/icce.v21.34>
- Mathisen, P. P., & Madsen, O. S. (1999). Waves and currents over a fixed rippled bed: 3. Bottom and apparent roughness for spectral waves and currents. *Journal of Geophysical Research*, 104(C8), 18447–18461. <https://doi.org/10.1029/1999jc900114>
- Michaud, H., Marsaleix, P., Leredde, Y., Estournel, C., Bourrin, F., Lyard, F., et al. (2012). Three-dimensional modelling of wave-induced current from the surf zone to the inner shelf. *Ocean Science*, 8(4), 657–681. <https://doi.org/10.5194/os-8-657-2012>
- Moghim, S., Thomson, J., Özkan-Haller, T., Umlauf, L., & Zippel, S. (2016). On the modeling of wave-enhanced turbulence nearshore. *Ocean Modelling*, 103, 118–132. <https://doi.org/10.1016/j.ocemod.2015.11.004>
- Morgan, S. G., Shanks, A. L., MacMahan, J. H., Reniers, A. J., & Feddersen, F. (2018). Planktonic subsidies to surf-zone and intertidal communities. *Annual Review of Marine Science*, 10, 345–369. <https://doi.org/10.1146/annurev-marine-010816-060514>
- Mouragues, A., Bonneton, P., Lannes, D., Castelle, B., & Marieu, V. (2019). Field data-based evaluation of methods for recovering surface wave elevation from pressure measurements. *Coastal Engineering*, 150, 147–159. <https://doi.org/10.1016/j.coastaleng.2019.04.006>
- Nairn, R. B., Roelvink, J., & Southgate, H. N. (1991). Transition zone width and implications for modelling surfzone hydrodynamics. *Coastal Engineering*, 1990, 68–81. <https://doi.org/10.1061/9780872627765.007>
- Nicolae-Lerma, A., Bulteau, T., Lecacheux, S., & Idier, D. (2015). Spatial variability of extreme wave height along the atlantic and channel French coast. *Ocean Engineering*, 97, 175–185. <https://doi.org/10.1016/j.oceaneng.2015.01.015>
- Noyes, T. J., Guza, R., Elgar, S., & Herbers, T. (2004). Field observations of shear waves in the surf zone. *Journal of Geophysical Research*, 109(C1), C01031. <https://doi.org/10.1029/2002jc001761>
- Oltman-Shay, J., Howd, P., & Birkemeier, W. (1989). Shear instabilities of the mean longshore current: 2. Field observations. *Journal of Geophysical Research*, 94(C12), 18031–18042. <https://doi.org/10.1029/jc094ic12p18031>
- Paskyabi, M. B., Fer, I., & Jenkins, A. D. (2012). Surface gravity wave effects on the upper ocean boundary layer: Modification of a one-dimensional vertical mixing model. *Continental Shelf Research*, 38, 63–78. <https://doi.org/10.1016/j.csr.2012.03.002>
- Pezerat, M., Bertin, X., Martins, K., & Lavaud, L. (2022). *Cross-shore distribution of the wave-induced circulation over a dissipative beach under storm wave conditions: The dataset*. <https://doi.org/10.5281/zenodo.5878857>
- Pezerat, M., Bertin, X., Martins, K., Mengual, B., & Hamm, L. (2021). Simulating storm waves in the nearshore area using spectral model: Current issues and a pragmatic solution. *Ocean Modelling*, 158, 101737. <https://doi.org/10.1016/j.ocemod.2020.101737>
- Rasche, N. (2007). *Impact of waves on the ocean circulation* (Unpublished doctoral dissertation). Université de Bretagne Occidentale.
- Reniers, A. J., Roelvink, J., & Thornton, E. (2004). Morphodynamic modeling of an embayed beach under wave group forcing. *Journal of Geophysical Research*, 109(C1), C01030. <https://doi.org/10.1029/2002jc001586>
- Roland, A., Zhang, Y. J., Wang, H. V., Meng, Y., Teng, Y.-C., Maderich, V., & Zanke, U. (2012). A fully coupled 3d wave-current interaction model on unstructured grids. *Journal of Geophysical Research*, 117(C11), C00J33. <https://doi.org/10.1029/2012jc007952>
- Saha, S., Moorthi, S., Wu, X., Wang, J., Nadiga, S., Tripp, P., & Becker, E. (2011). *Ncep climate forecast system version 2 (cfsv2) selected hourly time-series products*. Boulder CO: Research Data Archive at the National Center for Atmospheric Research, Computational and Information Systems Laboratory. <https://doi.org/10.5065/D6N877VB>
- Smith, J. A. (2006). Wave–current interactions in finite depth. *Journal of Physical Oceanography*, 36(7), 1403–1419. <https://doi.org/10.1175/jpo2911.1>
- Stive, M., & Wind, H. (1986). Cross-shore mean flow in the surf zone. *Coastal Engineering*, 10(4), 325–340. [https://doi.org/10.1016/0378-3839\(86\)90019-0](https://doi.org/10.1016/0378-3839(86)90019-0)
- Svendsen, I. A. (1984a). Mass flux and undertow in a surf zone. *Coastal Engineering*, 8(4), 347–365. [https://doi.org/10.1016/0378-3839\(84\)90030-9](https://doi.org/10.1016/0378-3839(84)90030-9)

- Svendsen, I. A. (1984b). Wave heights and set-up in a surf zone. *Coastal Engineering*, 8(4), 303–329. [https://doi.org/10.1016/0378-3839\(84\)90028-0](https://doi.org/10.1016/0378-3839(84)90028-0)
- Tajima, Y., & Madsen, O. S. (2006). Modeling near-shore waves, surface rollers, and undertow velocity profiles. *Journal of Waterway, Port, Coastal, and Ocean Engineering*, 132(6), 429–438. [https://doi.org/10.1061/\(asce\)0733-950x\(2006\)132:6\(429\)](https://doi.org/10.1061/(asce)0733-950x(2006)132:6(429))
- Tolman, H. L. (1991). A third-generation model for wind waves on slowly varying, unsteady, and inhomogeneous depths and currents. *Journal of Physical Oceanography*, 21(6), 782–797. [https://doi.org/10.1175/1520-0485\(1991\)021<0782:atgmfw>2.0.co;2](https://doi.org/10.1175/1520-0485(1991)021<0782:atgmfw>2.0.co;2)
- Tolman, H. L. (1994). Wind waves and movable-bed bottom friction. *Journal of Physical Oceanography*, 24, 994–1009. [https://doi.org/10.1175/1520-0485\(1994\)024<0994:wwambb>2.0.co;2](https://doi.org/10.1175/1520-0485(1994)024<0994:wwambb>2.0.co;2)
- Uchiyama, Y., McWilliams, J. C., & Shchepetkin, A. F. (2010). Wave–current interaction in an oceanic circulation model with a vortex-force formalism: Application to the surf zone. *Ocean Modelling*, 34(1–2), 16–35. <https://doi.org/10.1016/j.ocemod.2010.04.002>
- Umlauf, L., & Burchard, H. (2003). A generic length-scale equation for geophysical turbulence models. *Journal of Marine Research*, 61(2), 235–265. <https://doi.org/10.1357/002224003322005087>
- Umlauf, L., Burchard, H., & Bolding, K. (2005). *The general ocean turbulence model (gotm) scientific documentation: Version 3.2* (Technical Report No. 63). Warnemunde, Germany: Leibniz Institute for Baltic Sea Research.
- Wang, P., McWilliams, J. C., Uchiyama, Y., Chekroun, M. D., & Yi, D. L. (2020). Effects of wave streaming and wave variations on nearshore wave-driven circulation. *Journal of Physical Oceanography*, 50(10), 3025–3041. <https://doi.org/10.1175/jpo-d-19-0304.1>
- Wright, L. D., & Short, A. D. (1984). Morphodynamic variability of surf zones and beaches: A synthesis. *Marine Geology*, 56(1–4), 93–118. [https://doi.org/10.1016/0025-3227\(84\)90008-2](https://doi.org/10.1016/0025-3227(84)90008-2)
- Xu, Z., & Bowen, A. (1994). Wave-and wind-driven flow in water of finite depth. *Journal of Physical Oceanography*, 24(9), 1850–1866. [https://doi.org/10.1175/1520-0485\(1994\)024<1850:wawdfi>2.0.co;2](https://doi.org/10.1175/1520-0485(1994)024<1850:wawdfi>2.0.co;2)
- Zhang, H., Madsen, O. S., Sannasiraj, S., & Chan, E. S. (2004). Hydrodynamic model with wave–current interaction in coastal regions. *Estuarine, Coastal and Shelf Science*, 61(2), 317–324. <https://doi.org/10.1016/j.ecss.2004.06.002>
- Zhang, Y. J., Ye, F., Stanev, E. V., & Grashorn, S. (2016). Seamless cross-scale modeling with schism. *Ocean Modelling*, 102, 64–81. <https://doi.org/10.1016/j.ocemod.2016.05.002>
- Zheng, P., Li, M., van der Zanden, J., Wolf, J., Chen, X., Wang, C., & Wang, C. (2017). A 3D unstructured grid nearshore hydrodynamic model based on the vortex force formalism. *Ocean Modelling*, 116, 48–69. <https://doi.org/10.1016/j.ocemod.2017.06.003>